

# **WAVE OVERTOPPING AND DAMAGE PROGRESSION ON RUBBLE MOUND STRUCTURES**

by

Ali Farhadzadeh, Nobuhisa Kobayashi and Jeffrey Melby

Research Report No. CACR-09-05  
December 2009



Center for Applied Coastal Research  
University of Delaware  
Newark, DE 19716

## **ACKNOWLEDGEMENT**

This study was supported by the U.S. Army Corps of Engineers, Coastal and Hydraulics Laboratory under Contract No. W912HZ-08-P-0342 and W912BU-09-C-0023.

## TABLE OF CONTENTS

<b>LIST OF TABLES.....</b>	<b>V</b>
<b>LIST OF FIGURES.....</b>	<b>VII</b>
<b>ABSTRACT.....</b>	<b>XI</b>
<b>CHAPTER 1 INTRODUCTION.....</b>	<b>1</b>
<b>CHAPTER 2 TIME-AVERAGED PROBABILISTIC MODEL FOR PERMEABLE WET AND DRY ZONE.....</b>	<b>5</b>
<b>2.1 MODEL DESCRIPTION.....</b>	<b>5</b>
<b>2.2 GOVERNING EQUATIONS.....</b>	<b>8</b>
<b>2.3 COMPUTATIONAL PROCEDURE.....</b>	<b>19</b>
<b>CHAPTER 3 COMPARISON OF MODEL WITH WAVE OVERTOPPING DATA.....</b>	<b>20</b>
<b>3.1 SEEPAGE TESTS.....</b>	<b>21</b>
<b>3.2 COMBINED WAVE OVERTOPPING AND SEEPAGE TESTS.....</b>	<b>23</b>
<b>3.3 WAVE OVERTOPPING TESTS.....</b>	<b>25</b>
<b>3.4 TESTS BY VAN GENT.....</b>	<b>27</b>
<b>3.5 MODEL CALIBRATION.....</b>	<b>30</b>
<b>3.6 COMPARISON OF CALIBRATED MODEL WITH DATA.....</b>	<b>34</b>
<b>3.7 PERMEABILITY EFFECTS.....</b>	<b>53</b>

<b>CHAPTER 4</b>	<b>DAMAGE PROGRESSION MODEL FOR ARMOR LAYER.....</b>	<b>65</b>
<b>CHAPTER 5</b>	<b>COMPARISON OF DAMAGE PROGRESSION MODEL WITH DATA.....</b>	<b>70</b>
5.1	EXPERIMENT BY MELBY AND KOBAYASHI.....	70
5.2	MODEL CALIBRATION.....	72
5.3	COMPARISON WITH DAMAGE TESTS.....	80
<b>CHAPTER 6</b>	<b>CONCLUSIONS.....</b>	<b>91</b>
<b>REFERENCES.....</b>		<b>93</b>

## LIST OF TABLES

Table 3-1. Structure and Armor Layer Characteristics for Four Test Series.....	21
Table 3-2. Wave Conditions and Still Water Level at $x = 0$ for Test Series S.....	23
Table 3-3. Wave Conditions and Still Water Level at $x = 0$ for Test Series OS.....	25
Table 3-4. Wave Conditions and Still Water Level at $x = 0$ for Test Series O.....	27
Table 3-5. Wave Conditions and Still Water Level at $x = 0$ for Test Series D'.....	29
Table 3-6. Measured and Computed Wave Overtopping Probabilities and Rates for D' Test Series.....	37
Table 3-7. Computed Wave Overtopping Probability and Measured and Computed Rates for S Test Series .....	38
Table 3-8. Computed Wave Overtopping Probability and Measured and Computed Rates for OS Test series.....	39
Table 3-9. Measured and Computed Wave Overtopping Probabilities and Rates for O Test series.....	40
Table 3-10. Computed Wave Overtopping Probability and Rate with IPERM=0 and 1 for D' Test Series.....	56
Table 3-11. Computed Wave Overtopping Probability and Rate with IPERM=0 and 1 for S Test Series.....	57

Table 3-12. Computed Wave Overtopping Probability and Rate with IPERM=0 and 1 for OS Test Series.....	58
Table 3-13. Computed Wave Overtopping Probability and Rate with IPERM=0 and 1 for O Test Series.....	59
Table 5-1. Still Water Level and Wave Conditions at $x = 0$ for Three Damage Progression Tests.....	72

## LIST OF FIGURES

Fig.2-1. Transition from wet model ( $x < x_r$ ) to wet and dry model ( $x > x_{SWL}$ ) on permeable stone layer.....	6
Fig.2-2. Flow variables in porous wet and dry zone.....	9
Fig.2-3. Function $G_b(r)$ for wet and dry zone.....	17
Fig.3-1. Seepage (S) tests with permeable 1/5 slope.....	22
Fig.3-2. Combined overtopping and seepage (OS) tests with permeable 1/5 slope.....	24
Fig.3-3. Overtopping (O) tests with permeable 1/2 slope.....	26
Fig.3-4. $D'$ tests conducted by van Gent (2002) .....	28
Fig.3-5. Comparison of measured and computed wave overtopping rates for $\gamma = 0.7, 0.8$ and $0.9$ .....	31
Fig.3-6. Comparison of measured and computed wave overtopping rates for $\alpha_m = 0$ .....	32
Fig.3-7. Comparison of measured and computed wave overtopping probabilities for $\alpha_m = 0$ .....	33
Fig.3-8. Comparison of measured and computed wave overtopping rates for $\mu = 0.1, 0.3$ and $1$ .....	34
Fig.3-9. Comparison of measured and computed wave overtopping rates.....	35
Fig.3-10. Comparison of measured and computed wave overtopping probabilities.....	36

Fig.3-11.Spatial variations of mean water level, free surface standard deviation, mean velocity, velocity standard deviation and wet probability for D'5 test.....	42
Fig.3-12.Spatial variations of mean water level, free surface standard deviation, mean velocity, velocity standard deviation and wet probability for D'10 test.....	43
Fig.3-13.Spatial variations of mean water level, free surface standard deviation, mean velocity, velocity standard deviation and wet probability for S11 test.....	44
Fig.3-14.Spatial variations of mean water level, free surface standard deviation, mean velocity, velocity standard deviation and wet probability for OS3 test.....	45
Fig.3-15.Spatial variations of mean water level, free surface standard deviation, mean velocity, velocity standard deviation and wet probability for O9 test.....	46
Fig.3-16.Comparison of measured and computed cross-shore variations of $h_{2\%}$ , $U_{2\%}$ and $q_{2\%}$ for D'5 test.....	49
Fig.3-17.Comparison of measured and computed cross-shore variations of $h_{2\%}$ , $U_{2\%}$ and $q_{2\%}$ for D'10 test.....	50
Fig.3-18.Comparison of measured and computed values of $h_{2\%}$ for D' test series.....	51
Fig.3-19.Comparison of measured and computed values of $U_{2\%}$ for D' test series.....	52
Fig.3-20.Comparison of measured and computed values of $q_{2\%}$ for D' test series.....	53
Fig.3-21.Comparison of measured and computed wave overtopping rates for IPERM=0.....	54
Fig.3-22.Comparison of measured and computed wave overtopping probabilities for IPERM=0.....	55

Fig.3-23.Comparison of mean water level, free surface standard deviation, mean velocity, velocity standard deviation and wet probability for permeable and impermeable bottoms for D'5 test.....	60
Fig.3-24.Comparison of mean water level, free surface standard deviation, mean velocity, velocity standard deviation and wet probability for permeable and impermeable bottoms for D'10 test.....	61
Fig.3-25.Comparison of mean water level, free surface standard deviation, mean velocity, velocity standard deviation and wet probability for permeable and impermeable bottoms for S11 test .....	62
Fig.3-26.Comparison of mean water level, free surface standard deviation, mean velocity, velocity standard deviation and wet probability for permeable and impermeable bottoms for OS3 test.....	63
Fig.3-27.Comparison of mean water level, free surface standard deviation, mean velocity, velocity standard deviation and wet probability for permeable and impermeable bottoms for O9 test.....	64
Fig.4-1.Bottom slope function $G_s$ versus bottom slope.....	69
Fig.5-1.Experimental setup for damage progression tests.....	71
Fig.5-2.Comparison of final damage profile for test A', for $m=0.5, 1$ and $2$ .....	73
Fig.5-3.Comparison of final damage profile for test B', for $m=0.5, 1$ and $2$ .....	74
Fig.5-4.Comparison of final damage profile for test C', for $m=0.5, 1$ and $2$ .....	75
Fig.5-5.Damage progression for tests A', B' and C' for $m=0.5, 1$ and $2$ .....	76
Fig.5-6.Comparison of final damage profile for test A', for $N_c =0.6, 0.7$ and $0.8$ .....	77

Fig.5-7.Comparison of final damage profile for test B', for $N_c = 0.6, 0.7$ and $0.8$ .....	78
Fig.5-8.Comparison of final damage profile for test C', for $N_c = 0.6, 0.7$ and $0.8$ .....	79
Fig.5-9.Damage progression for tests A', B' and C' for $N_c = 0.6, 0.7$ and $0.8$ .....	80
Fig.5-10.Measured and computed damage profile for test A' at $t = 10.5 h, 17.5 h$ and 28.5 h .....	82
Fig.5-11.Measured and computed damage profile for test B' at $t = 4.5 h$ and $8.5 h$ ....	83
Fig.5-12.Measured and computed damage profile for test C' at $t = 5 h$ and $9 h$ .....	84
Fig.5-13.Temporal variation of damage, overtopping rate, root-mean-square wave height and still water level for test A'.....	85
Fig.5-14.Temporal variation of damage, overtopping rate, root-mean-square wave height and still water level for test B'.....	86
Fig.5-15.Temporal variation of damage, overtopping rate, root-mean-square wave height and still water level for test C'.....	87
Fig.5-16.Armor profile evolution for test A'.....	88
Fig.5-17.Armor profile evolution for test B'.....	89
Fig.5-18.Armor layer evolution for test C'.....	90

## ABSTRACT

A probabilistic hydrodynamic model for the wet and dry zone on a permeable structure is developed to predict irregular wave action on the structure above the still water level. The model is based on the time-averaged continuity and momentum equations for nonlinear shallow-water waves coupled with the exponential probability distribution of the water depth. The model predicts the cross-shore variations of the mean and standard deviation of the water depth and horizontal velocity. The model is compared with four test series in which measurement was made of the wave overtopping rate and probability as well as the water depth, velocity and discharge exceeded by 2% of incident 1,000 waves. The agreement is mostly within a factor of 2.

Damage progression of a stone armor layer is predicted by modifying a formula for bed load on beaches with input from the hydrodynamic model. The damage progression model is compared with three tests by Melby and Kobayashi (1998) that lasted up to 28.5 hours. The model predicts the eroded area of the damaged armor layer well but overpredicts the deposited area because it does not account for discrete stone units deposited at a distance seaward of the toe of the damaged armor layer. The model predicts the temporal progression of the eroded area quite well. The numerical model is very efficient and suited for a risk-based design of rubble mound structures.

# **CHAPTER 1**

## **INTRODUCTION**

Rubble mound structures are widely used to protect the landward area including a port or harbor against wave attack mostly because they dissipate wave energy more effectively than impermeable structures.

Design of rubble mound breakwaters has always been challenging because the wave hydrodynamics near and on the structures alters during storms as the profile of the breakwater changes. The design of a rubble mound structure requires the hydrodynamic prediction of wave overtopping over its crest and the damage prediction of its armor layer (Coastal Engineering Manual 2003). These two predictions are related but made separately because the profile evolution of the damaged armor layer cannot be predicted presently. The damage progression and the increase of wave overtopping will need to be predicted in order to assess the performance of the structure during an entire storm. Such a comprehensive model is developed here to aid a risk-based design of the rubble mound structure.

A number of time-dependent hydrodynamic models for rubble mound structures have already been developed as reviewed by Losada et al. (2008). These numerical models try to predict the temporal and spatial variations of wave dynamics as accurately as possible. The computation time normally increases with the increase of the resolution and accuracy. The computationally advanced models are used to predict hydrodynamic variables for relatively short durations. To reduce computation time considerably, Kobayashi et al. (2007) proposed a probabilistic model. The time-varying wave variables are expressed using a probability distribution. The spatial variations of the mean and standard deviation are computed using the time-averaged governing equations. The probabilistic time-averaged model requires additional assumptions but its computational efficiency allows the calibration of the model parameters using a large number of tests. The model was developed to include wave and current interaction (Farhadzadeh et al. 2007). Later, the probabilistic model was extended to the wet and dry zone in order to predict wave runup and overtopping (Kobayashi and Farhadzadeh 2008).

In the present report, the probabilistic model for the wet and dry zone is expanded to include the permeability effects. The new model is capable of predicting the wave and flow motion above and inside the permeable armor layer in the wet and dry zone. The probabilistic model for the permeable wet and dry model coupled with the permeable wet model can predict the irregular wave evolution and the flow hydrodynamic from the offshore boundary to the landward end of a rubble mound

structure. The extended model provides the hydrodynamic input to a damage progression model that predicts the slow evolution of an armor layer profile.

Kobayashi and Otta (1987) developed a time-dependent model to predict the stone movement under regular wave attack. The model utilized the equation of motion for each individual armor unit in order to estimate the stone movement. The profile evolution of the armor layer may then be predicted by computing the displacements of all the armor units (Norton and Holmes 1992). However, this approach has never been adopted for practical applications probably because of its computation time.

In the present study, the sediment transport model developed by Kobayashi et al. (2009) is modified to predict the evolution of the armor layer profile. The armor layer evolution is predicted in manners similar to the prediction of sandy beach profile evolution. Even though this simple approach neglects the discrete nature of armor stone units, it is very convenient for the prediction of the armor layer profile evolution averaged alongshore where the alongshore averaging reduces the discrete nature.

The present report is organized in the following chapters:

In Chapter 2, the probabilistic time-averaged model for the wet zone on a permeable bottom is extended to the permeable wet and dry zone.

In Chapter 3, the hydrodynamic model extended to the wet and dry zone is compared with wave overtopping data of 52 tests.

In Chapter 4, the damage progression model for the armor layer, based on the sediment transport model, is explained.

In Chapter 5, the armor layer evolution model is compared with three damage progression tests.

Finally, in Chapter 6 the conclusions are presented.

It is noted that the summary of this report is presented by Farhadzadeh, Kobayashi and Melby (2010) and Kobayashi, Farhadzadeh and Melby (2010).

## **CHAPTER 2**

# **TIME-AVERAGED PROBABILISTIC MODEL FOR PERMEABLE WET AND DRY ZONE**

The wet model for both permeable and impermeable bottoms is elaborated in the report by Kobayashi and Farhadzadeh (2008). In this Chapter, the time-averaged probabilistic model for the porous wet and dry zone is explained. The permeable wet and dry model in connection with the wet model is used to predict the wave hydrodynamics such as the mean water depth and velocity and the standard deviations of the water depth and velocity above the porous layer. The computed hydrodynamic parameters are utilized to predict the stone movement in order to predict the damage progression of rubble mound structures.

### **2.1. Model Description**

The numerical model assumes that the incident waves are normal to the structure which is uniform in the longshore direction. Fig. 2-1 shows the flow above a permeable slope. As Fig. 2-1 displays, the origin of the cross-shore coordinate system is located at the offshore

boundary with the positive on-shore directed  $x$ -coordinate. The vertical coordinate  $z$  is taken to be positive upward where the datum is  $z = 0$ .

The still water level (SWL) above the datum denoted as  $S$  in Fig. 2-1 is allowed to vary in time during a storm or an experiment. The upper and lower boundaries of the permeable stone layer are located at  $z = z_b(x)$  and  $z_p(x)$ , respectively, where the lower boundary is assumed to be impermeable to simplify the analysis. The crest height  $R_c$  is taken conventionally as the structure height above SWL. The crest location  $x_c$  is defined here as the highest and most landward location. The wave overtopping rate is denoted as  $q_o$ . The SWL shoreline on the seaward slope is located at  $x_{SWL}$ . The mean water level (MWL) is located at  $z = (S + \bar{\eta})$  where  $\bar{\eta}$  is the wave setup above SWL. The mean water depth  $\bar{h}$  above  $z = z_b$  is given by  $\bar{h} = (S + \bar{\eta} - z_b)$ . The cross-shore location  $x_r$  is the landward limit of the time-averaged model in the wet zone.

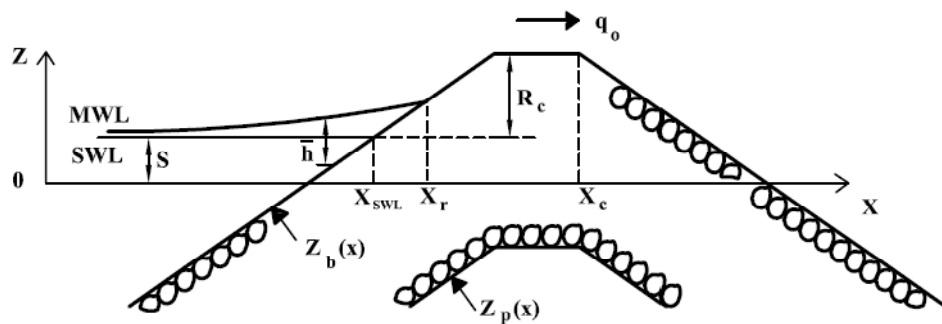


Fig. 2-1. Transition from wet model ( $x < x_r$ ) to wet and dry model ( $x > x_{SWL}$ ) on permeable stone layer

The time-averaged model for the wet permeable slope developed by Kobayashi et al. (2007) is modified using linear wave and current theory (e.g., Mei 1989) where wave overtopping induces onshore current. The time-averaged continuity, momentum, and wave action equations are used to predict the cross-shore variations of the mean  $\bar{U}$  of the depth-averaged cross-shore velocity  $U$ , the mean  $\bar{\eta}$  of the free surface elevation  $\eta$  above SWL, and the free surface standard deviation  $\sigma_\eta$ . The overbar denotes time averaging. The root-mean-square (RMS) wave height is defined as  $H_{\text{rms}} = \sqrt{8} \sigma_\eta$ . Linear progressive wave theory is used locally to express the velocity standard deviation  $\sigma_U$  in terms of  $\sigma_\eta$ . The probability distributions of  $\eta$  and  $U$  are assumed to be Gaussian. The equivalency of the time averaging and probabilistic averaging is assumed to express the time-averaged terms in the governing equations in terms of  $\bar{\eta}$ ,  $\sigma_\eta$ ,  $\bar{U}$  and  $\sigma_U$ . The permeability effects are included in the same way as in Kobayashi et al. (2007).

The equations used for the present computation are presented in the report by Kobayashi and Farhadzadeh (2008). The landward-marching computation using this model for the wet zone is continued as long as the computed  $\bar{h}$  and  $\sigma_\eta$  are larger than 0.1 cm. The end location of the computation is denoted as  $x_r$  in Fig. 2-1. The time-average model for the wet zone cannot predict wave overtopping. Consequently, Kobayashi and de los Santos (2007) relied on empirical formulas for wave overtopping and seepage rates. In this report, a separate model for the wet and dry zone is developed and connected with the model for the wet zone. This procedure is the same as that used by Kobayashi et al. (2010) for impermeable structures.

## 2.2. Governing Equations

Fig. 2-2 depicts the flow pattern above and inside a permeable layer and the variables used in the following. The time-averaged cross-shore continuity and momentum equations derived from the nonlinear shallow-water wave equations on the permeable slope (Wurjanto and Kobayashi 1993) are expressed as

$$\frac{d}{dx}(\overline{hU}) = -\overline{w_p} \quad (2-1)$$

$$\frac{d}{dx}\left(\overline{hU^2} + \frac{g}{2}\overline{h^2}\right) = -g\overline{h}\frac{dz_b}{dx} - \frac{1}{2}f_b\overline{|U|U} - \overline{u_b w_p} \quad (2-2)$$

where  $h$  and  $U$  = instantaneous water depth and cross-shore velocity, respectively;  $w_p$  = vertical seepage velocity which is taken to be positive downward;  $g$  = gravitational acceleration;  $z_b$  = bottom elevation above the datum  $z=0$ ;  $f_b$  = bottom friction factor which is allowed to vary spatially; and  $u_b$  = horizontal fluid velocity at  $z = z_b$ . The last term on the right hand side of Eq. (2-2) represents the time-averaged flux of the horizontal momentum into the permeable layer. The overbar in Eqs.(2-1) and (2-2) for the wet and dry zone indicates averaging for the wet duration only because no water exists during the dry duration.

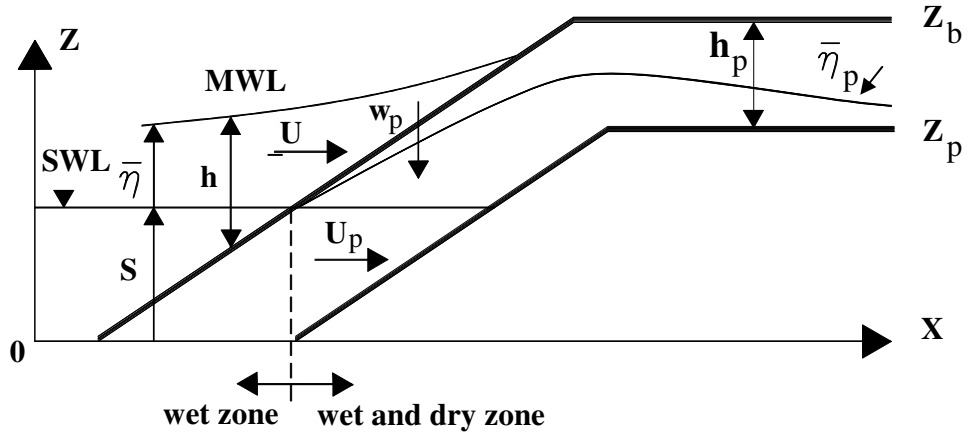


Fig. 2-2. Flow variables in the porous wet and dry zone

The continuity and approximate momentum equations for the flow inside the permeable layer are expressed as

$$\frac{dq_p}{dx} = \overline{w_p} \quad (2-3)$$

$$\left( \alpha_p + \beta_1 |\overline{U_p}| \right) \overline{U_p} = -g \frac{d\overline{\eta}}{dx} \quad (2-4)$$

with

$$\alpha_p = 1000 \left( \frac{1-n_p}{n_p} \right)^2 \frac{\nu}{D_{n50}^2} ; \beta_1 = \frac{5(1-n_p)}{D_{n50} n_p^3} \quad (2-5)$$

where  $q_p$  = time-averaged horizontal volume flux in the permeable layer;  $\overline{U_p}$  = time-averaged horizontal discharge velocity;  $\alpha_p$  and  $\beta_1$  = coefficients associated with the laminar and

turbulent flow resistance, respectively;  $n_p$  = porosity of the permeable layer;  $D_{n50}$  = nominal stone diameter; and  $\nu$  = kinetic viscosity of the fluid. Eq. (2-5) is based on the formula developed by van Gent (1995) and calibrated by Kobayashi et al. (2007). The resistance component associated with the oscillatory flow is simply neglected in Eq. (2-4) which is solved analytically to obtain the discharge velocity  $\overline{U}_p$  driven by the horizontal pressure gradient due to  $\overline{\eta} = (\overline{h} + z_b - S)$  where  $\overline{h}$  and  $z_b$  vary with  $x$ . It is noted that Eq. (2-4) retains only the leading terms in the horizontal momentum equation given by Wurjanto and Kobayashi (1993).

Adding Eqs. (2-1) and (2-3) and integrating the resulting equation with respect to  $x$ , the vertically integrated continuity equation is obtained

$$\overline{hU} + q_p = q_o \quad (2-6)$$

where the wave overtopping rate  $q_o$  is defined in this report as the sum of the volume fluxes above and inside the permeable layer. The volume flux  $q_p$  is estimated as

$$q_p = P_w \overline{U}_p (\overline{\eta}_p - z_p) \quad (2-7)$$

where  $P_w$  = wet probability defined as the ratio between the wet and entire durations:  $\overline{\eta}_p$  = average water level inside the permeable layer; and  $z_p$  = elevation of the impermeable lower boundary. To estimate the volume flux  $q_p$  in Eq. (2-7),  $\overline{U}_p$  is obtained using Eq. (2-4). In addition, the mean water level inside the permeable layer  $\overline{\eta}_p$  needs to be predicted. The

elevation  $\bar{\eta}_p$  and  $z_p$  are relative to the datum  $z = 0$  in Fig. 2-2 and  $(\bar{\eta}_p - z_p)$  is the thickness of water inside the permeable layer. The elevation  $\bar{\eta}_p$  is estimated as

$$\bar{\eta}_p = P_w z_b + (1 - P_w) z_p \quad \text{for } z_p \geq S \quad (2-8)$$

$$\bar{\eta}_p = P_w z_b + (1 - P_w) S \quad \text{for } z_p < S \quad (2-9)$$

The upper bound of  $\bar{\eta}_p$  for  $P_w = 1$  is the upper boundary of the permeable layer located at  $z = z_b$ . The lower bound of  $\bar{\eta}_p$  for  $P_w = 0$  is the higher elevation of the lower boundary  $z_p$  of the permeable layer and the still water level  $S$ . The wet probability  $P_w$  in Eq. (2-7) ensures that  $q_p = 0$  if  $P_w = 0$ . Eqs. (2-7) – (2-9) based on physical reasoning may be crude but are used along with Eqs. (2-4) and (2-5) to estimate  $q_p$  for the known  $\bar{h}$  and  $P_w$ .

A few attempts were made to estimate the time-averaged flux of the horizontal momentum into the permeable layer in Eq. (2-2). Initially, the term  $\overline{u_b w_p}$  was ignored, which resulted in the overestimation of the wave overtopping rate especially for two test series with a thick permeable layer. Accordingly, the momentum flux into the permeable layer is included in the momentum equation. The term  $\overline{u_b w_p}$  is expressed as

$$\overline{u_b w_p} = m \sqrt{g \bar{h}} \bar{w}_p \quad (2-10)$$

where  $\bar{w}_p = dq_p/dx$  is the mean vertical seepage velocity into the permeable layer. The parameter  $m$  was considered to be constant. No contribution of the exfiltrated flow for the

momentum equation was included because the exfiltration velocity is normally small. Eq. (2-10) can be rewritten as

$$\overline{u_b w_p} = g \bar{h} P ; P = m \frac{\overline{w_p}}{\sqrt{g \bar{h}}} \quad (2-11)$$

The parameter  $P$  was calibrated but the agreement between the computed and measured overtopping and seepage rates for four test series was poor. In short, Eqs.(2-10) and (2-11) were not promising and abandoned.

In order to account for both permeable layer thickness and wet probably, the last term in Eq. (2-2) is expressed as

$$\overline{u_b w_p} = \alpha_m P_w (g \bar{h})^{0.5} w_m \quad (2-12)$$

with

$$(\alpha_p + \beta_1 w_m) w_m = g \quad (2-13)$$

where  $\alpha_m$  =empirical parameter which will be calibrated in Chapter 3; and  $w_m$  = maximum downward seepage velocity due to the gravity force. Eq. (2-13) is solved analytically

$$w_m = \frac{\sqrt{\alpha_p^2 + 4g\beta_1} - \alpha_p}{2\beta_1} \quad (2-14)$$

The seepage velocity  $w_p$  is assumed to be of the order of  $w_m$  or less. The horizontal velocity  $u_b$  at  $z = z_b$  is assumed to be of the order of  $(g \bar{h})^{0.5}$ . Eq. (2-12) assumes that the downward flux of the horizontal momentum during the wet duration is much larger than the upward

momentum flux from the permeable layer. Therefore, the upward momentum flux is assumed to have no contribution to the momentum equation.

The cross-shore variation of the mean water depth  $\bar{h}$  is obtained by solving the momentum equation (2-2) together with the continuity equation (2-6). Kobayashi et al. (1998) studied the probability distributions of free surface elevations on a beach. They found that the probability distribution function  $f(h)$  in the lower swash zone can be presented in form of an exponential function. This assumption simplifies the cross-shore model in the wet and dry zone. The exponential probability density function  $f(h)$  is expressed as

$$f(h) = \frac{P_w^2}{h} \exp\left(-P_w \frac{h}{h}\right) \text{ for } h > 0 \quad (2-15)$$

with

$$P_w = \int_0^{\infty} f(h)dh \quad ; \quad \bar{h} = \int_0^{\infty} hf(h)dh \quad (2-16)$$

The wet probability  $P_w$  equals the probability of the instantaneous water depth  $h > 0$ . As a result, the dry probability of  $h = 0$  is equal to  $(1 - P_w)$ . The mean water depth for the wet duration is  $\bar{h}$  but the mean depth for the entire duration is equal to  $P_w \bar{h}$ .

The free surface elevation  $\eta$  above SWL is given by  $\eta = (h + z_b - S)$  where  $z_b$  and  $S$  are assumed to be invariant during the averaging. The standard deviations of  $\eta$  and  $h$  are the same and given by

$$\frac{\sigma_{\eta}}{h} = \left( \frac{2}{P_w} - 2 + P_w \right)^{0.5} \quad (2-17)$$

which yields  $\sigma_\eta = \bar{h}$  for  $P_w = 1$ . This equality was supported by the depth measurement in the lower swash zone by Kobayashi et al. (1998) who assumed  $P_w = 1$  in Eq. (2-15).

The cross-shore velocity  $U$  may be related to the depth  $h$  in the wet and dry zone and expressed as

$$U = \alpha\sqrt{gh} + U_s \quad (2-18)$$

where  $\alpha =$  positive constant; and  $U_s =$  steady velocity which is allowed to vary with  $x$ . The steady velocity  $U_s$  is included to account for offshore return flow on the seaward slope and crest and the downward velocity increase on the landward slope. Holland et al. (1991) measured the bore speed and flow depth on a barrier island using video techniques and obtained  $\alpha \simeq 2$  where the celerity and fluid velocity of the bore are assumed to be approximately the same. As a result, use may be made of  $\alpha \simeq 2$  as a first approximation. Based on Eq. (2-18), the cross-shore velocity in the wet and dry zone increases as the water depth increases and approaches the steady velocity  $U_s$  as the depth approaches zero. Using Eqs. (2-15) and (2-18), the mean  $\bar{U}$  and standard deviation  $\sigma_U$  of the cross-shore velocity  $U$  can be expressed as

$$\bar{U} = \frac{\sqrt{\pi}}{2} \alpha (P_w g \bar{h})^{0.5} + P_w U_s \quad (2-19)$$

$$\sigma_U^2 = \alpha^2 g \bar{h} - 2(\bar{U} - U_s)(\bar{U} - P_w U_s) + P_w (\bar{U} - U_s)^2 \quad (2-20)$$

Eqs. (2-17), (2-19) and (2-20) express  $\sigma_\eta$ ,  $\bar{U}$  and  $\sigma_U$  in terms of  $\bar{h}$ ,  $P_w$  and  $U_s$  which vary with  $x$ .

Eq. (2-18) is substituted into Eqs. (2-2) and (2-6) which are averaged for the wet duration using Eq. (2-15). The continuity equation (2-6) yields

$$\frac{3\sqrt{\pi}\alpha}{4}\bar{h}\left(\frac{g\bar{h}}{P_w}\right)^{0.5} + U_s\bar{h} = q \quad ; \quad q = q_o - q_p \quad (2-21)$$

where  $q$  = volume flux above the permeable layer. After lengthy algebra, the momentum equation (2-2) is expressed as

$$\frac{d}{dx}\left(B\frac{g\bar{h}^2}{P_w} + \frac{q^2}{h}\right) = -g\bar{h}\frac{dz_b}{dx} - \frac{f_b}{2}\alpha^2 g\bar{h}G_b(r) - \alpha_m P_w (g\bar{h})^{0.5} w_m \quad (2-22)$$

with

$$B = \left(2 - \frac{9\pi}{16}\right)\alpha^2 + 1 \quad ; \quad r = \frac{3\sqrt{\pi}}{4}\frac{U_s\bar{h}}{q - U_s\bar{h}} \quad (2-23)$$

where the parameter  $B$  is related to the momentum flux term on the left hand side of Eq. (2-2).

The function  $G_b(r)$  in Eq. (2-20) is given by

$$G_b(r) = 1 + \sqrt{\pi}r + r^2 \quad \text{for } r \geq 0 \quad (2-24)$$

$$G_b(r) = 2\exp(-r^2) - r^2 - 1 + \sqrt{\pi}r[2\text{erf}(r) + 1] \quad \text{for } r < 0 \quad (2-25)$$

where  $\text{erf}$  is the error function. The function  $G_b$  increases monotonically with the increase of  $r$  as shown in Fig. 2-3. The values of  $G_b$  are equal to 0 and 1 for  $r = -0.94$  and 0, respectively.

For  $r < -1.5$ ,  $G_b$  can be approximated as  $G_b \simeq -(1 + \sqrt{\pi}r + r^2)$ .

Eqs. (2-21) and (2-22) are used to predict the cross-shore variation of  $\bar{h}$  and  $U_s$  for assumed  $q_o$ . It is necessary to estimate the wet probability  $P_w$  empirically. To simplify the integration of Eq. (2-22), the following formula is adopted:

$$P_w = \left[ (1 + A_1) \left( \frac{\bar{h}_1}{\bar{h}} \right)^n - A \left( \frac{\bar{h}_1}{\bar{h}} \right)^3 \right]^{-1} ; A = \frac{q^2}{Bg\bar{h}_1^{-3}} ; A_1 = \frac{q_1^2}{Bg\bar{h}_1^{-3}} \quad (2-26)$$

where  $\bar{h}_1$  and  $q_1$  = mean water depth and volume flux, respectively, at the location of  $x = x_l$  where  $P_w = 1$ ;  $n$  = empirical parameter for  $P_w$ ; and  $A$  and  $A_1$  = dimensionless variables related to  $q$  and  $q_l$ , respectively. The transition from the wet ( $P_w = 1$  always) zone to the wet and dry ( $P_w < 1$ ) zone may be taken at  $x_l = x_{SWL}$  where  $x_{SWL}$  is the cross-shore location of the still water shoreline of an emerged crest as shown in Fig. 2-1. Eq. (2-26) is assumed to be valid on the upward slope and horizontal crest in the region of  $x_1 \leq x \leq x_c$  where  $x_c$  is the highest and most landward location of the structure. Eq (2-26) reduces to that used by Kobayashi et al. (2010) for an impermeable structure with  $q = q_l = q_o$ .

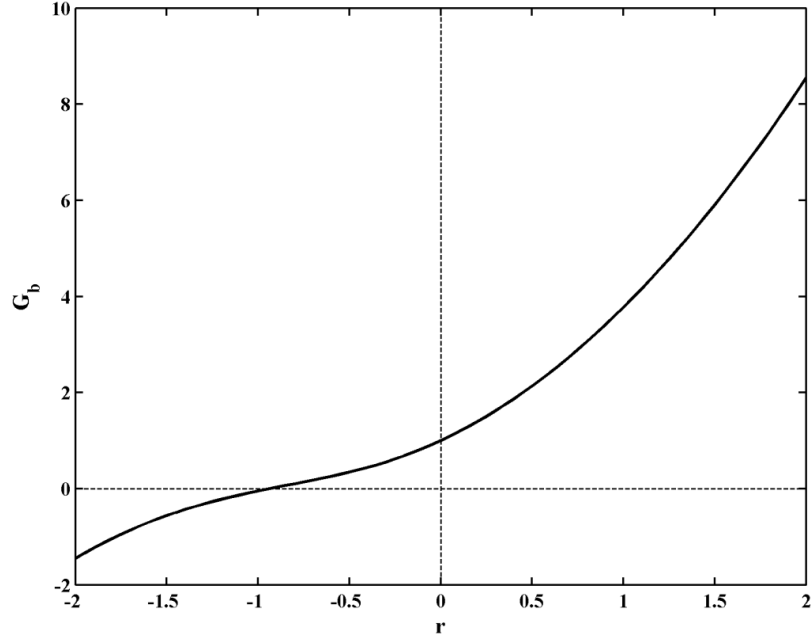


Fig. 2-3. Function  $G_b(r)$  for wet and dry zone

Integration of Eq. (2-22) for  $P_w$  given by Eq. (2-26) starting from  $\bar{h} = \bar{h}_1$  at  $x = x_1$  yields

$$B_n (1 + A_1) \bar{h}_1 \left[ \left( \frac{\bar{h}_1}{\bar{h}} \right)^{n-1} - 1 \right] = z_b(x) - z_b(x_1) + \int_{x_1}^x \left[ \frac{f_b}{2} \alpha^2 G_b + \alpha_m \frac{P_w W_m}{(g \bar{h})^{0.5}} \right] dx \quad (2-27)$$

where  $B_n = B(2 - n)/(n-1)$ ; and  $z_b(x)$  = bottom elevation at the cross-shore location  $x$ . The mean water depth  $\bar{h}$  at given  $x$  is computed by solving Eq. (2-27) iteratively. The empirical parameter  $n$  is taken to be in the range of  $1 < n < 2$  so that  $B_n > 0$ . The formula for  $n$  calibrated by Kobayashi et al. (2010) using 207 tests for wave overtopping of smooth impermeable structures is expressed as  $n = 1.01 + 0.98 \left[ \tanh(A_o) \right]^{0.3}$  where  $1.01 \leq n \leq 1.99$  and  $A_o = q_o^2 / (Bg \bar{h}_1^3)$ .

On the downward slope in the region of  $x > x_c$ , the wet probability  $P_w$  is assumed to be given by

$$P_w^{-1} = P_c^{-1} + \frac{q_c^2 - q^2}{Bg\bar{h}^{-3}} \quad (2-28)$$

where  $P_c$  and  $q_c$  are the computed wet probability  $P_w$  and volume flux  $q$  at  $x = x_c$ . For the case where the landward slope is impermeable,  $q = q_c = q_o$  and then  $P_w$  is equal to  $P_c$ .

Substituting Eq. (2-28) into Eq. (2-22) and integrating the resulting equation from  $x_c$  to  $x$ , the mean depth  $\bar{h}(x)$  is expressed as

$$\frac{\bar{h}}{h_c} - 1 + \frac{P_c q_c^2}{4gB\bar{h}_c^{-3}} \left[ \left( \frac{\bar{h}_c}{\bar{h}} \right)^2 - 1 \right] = \frac{P_c}{2B\bar{h}_c} \left\{ z_b(x_c) - z_b(x) - \int_{x_c}^x \left[ \frac{f_b}{2} \alpha^2 G_b + \alpha_m \frac{P_w W_m}{(gh)^{0.5}} \right] dx \right\} \quad (2-29)$$

where  $\bar{h}_c$  is the computed mean depth at  $x = x_c$ .

The wave overtopping rate  $q_o$  is predicted by imposing  $U_s = 0$  in Eq. (2-21) at the crest location  $x_c$

$$q_o = \frac{3\sqrt{\pi}\alpha}{4} \bar{h}_c \left( \frac{g\bar{h}_c}{P_c} \right)^{0.5} + q_p \quad \text{at } x = x_c \quad (2-30)$$

The wave overtopping probability  $P_o$  may be related to the wet probability  $P_c$  at  $x = x_c$  where both  $P_o$  and  $P_c$  are in the range of 0.0 – 1.0. The empirical relation of  $P_o = [\tanh(5P_c)]^{0.8}$  was fitted by Kobayashi et al. (2010) using 207 tests for wave overtopping of smooth impermeable structures.

### 2.3. Computational Procedure

For assumed  $q_o$ , the landward marching computation of  $\bar{h}, \sigma_\eta, \bar{U}$  and  $\sigma_U$  is initiated using the wet model from the seaward boundary  $x = 0$  to the landward limit located at  $x = x_r$ . The predicted mean depth at the location of  $x = x_{SWL}$  is taken as the boundary conditions for the wet and dry model. The landward marching computation is continued using the wet and dry model from the location of  $x = x_{SWL}$  where  $\bar{h} = \bar{h}_1$  and  $P_w=1$  to the landward end of the computation domain or until the mean depth  $\bar{h}$  becomes less than 0.001 cm. The rate  $q_o$  is computed using Eq. (2-30) together with the overtopping probability  $P_o$ . This landward computation starting from  $q_o = 0$  is repeated until the difference between the computed and assumed values of  $q_o$  is less than 1%. This convergency is normally obtained after several iterations. The computed values of  $\bar{h}, \sigma_\eta, \bar{U}$  and  $\sigma_U$  by the two different models in the overlapping zone of  $x_{SWL} < x < x_r$  are averaged to smooth the transition from the wet zone to the wet and dry zone.

## CHAPTER 3

# COMPARISON OF MODEL WITH WAVE OVERTOPPING DATA

In order to evaluate the numerical model for the permeable wet and dry zone in Chapter 2, the computed results are compared with the seepage (S) and overtopping and seepage (OS) test series (Kobayashi and de los Santos 2007), the overtopping (O) test series (Kobayashi and Raichle 1994), and the  $D'$  test series by van Gent (2002). The main characteristics of the armor layers and geometries of the four test series are summarized in Table 3-1. The number of tests varied in the range of 10 to 18. The seaward slope was in the range of 1/5 to 1/2. The symbols in Table 3-1 are defined as  $x_t$  = horizontal distance between the offshore boundary location  $x = 0$  and the toe of the structure;  $H_c$  = crest height of the structure above its toe;  $(S+R_c)$  = crest height above the datum  $z = 0$ ;  $D_{n50}$  = nominal stone diameter,  $t_a$  = maximum vertical thickness of the armor layer;  $w_m$  = maximum downward seepage velocity given by Eq. (2-14).

**Table 3-1.** Structure and Armor Layer Characteristics for Four Test Series

Test Series	Number of Tests	Structure				Armor Layer		
		Slope	$x_t$ (m)	$H_c$ (cm)	$(S + R_c)$ (cm)	$D_{n50}$ (cm)	$t_a$ (cm)	$w_m$ (cm/s)
S	12	1/5	6.3	39.1	18.6	3.40	14.0	12.8
OS	10	1/5	6.3	30.2	9.7	3.40	14.0	12.8
O	12	1/2	3.5	27.3	13.0	4.23	4.73	14.3
D'	18	1/4	0.0	60.5	30.5	0.49	0.49	4.4

### 3.1. Seepage Tests

Fig. 3-1 shows the experimental setup of the S test series. The number of tests was 12 and the tests were designed to measure the seepage rate through a 1/5 slope of a permeable stone layer with its vertical thickness  $h_p$  under irregular incident waves where  $t_a$  in Table 3-1 corresponds to the maximum value of  $h_p(x) = [z_b(x) - z_p(x)]$  (see Fig. 2-2). The crest height  $H_c$  of the structure above its toe was 39.1 cm. The crest height  $(S + R_c)$  above the datum  $z = 0$  (see Fig. 2-1) was 18.6 cm where the datum is taken as the lowest still water level in each test series. The nominal diameter, density and porosity of the stone were  $D_{n50}=3.4$  cm,  $\rho_s=2.95$  g/cm<sup>3</sup> and  $n_p=0.5$  respectively. The maximum downward seepage velocity  $w_m$  estimated using Eq. (2-14) along with Eq. (2-5) and  $\nu = 0.01$  cm<sup>2</sup>/s was 12.8 cm/s. The still water level  $S$ , root-mean-square (RMS) wave height  $H_{rms}$ , and spectral peak period  $T_p$  measured at the offshore boundary  $x = 0$  for each test are specified as input to the numerical model. The stationary profiles of  $z_b(x)$  and  $z_p(x)$  specified as input are the same for each test series where

$z_b = z_p$  in the zone of no permeable layer. The slope of the beach in front of the structure was 1/34.4. Table 3-2 summarizes the offshore boundary conditions of the waves and water level for the S tests. Three different peak periods of 2.3, 2.9 and 3.0 sec and six different root-mean-square wave heights of 7.3 - 11.9 cm were used. The offshore wave setup ranged from -0.27 cm to 0.8 cm. The still water level  $S$  was in the range of 0 - 4 cm.

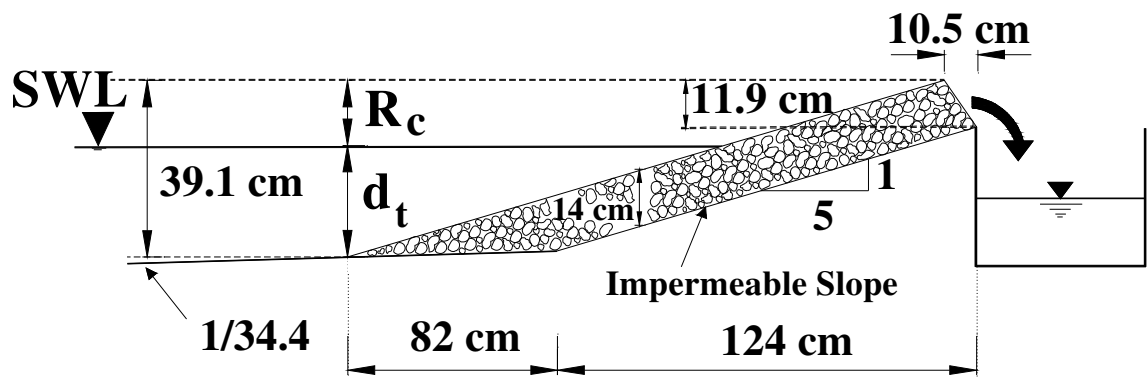


Fig. 3-1. Seepage (S) tests with permeable 1/5 slope

**Table 3-2.** Wave Conditions and Still Water Level at  $x = 0$  for Test Series S

Test No.	$T_p$ (sec)	$H_{rms}$ (cm)	$\bar{\eta}$ (cm)	S (cm)
1	2.3	11.2	0.28	0.0
2	2.3	11.2	0.26	0.0
3	3.0	7.3	0.17	0.0
4	3.0	7.3	0.24	0.0
5	2.3	11.6	0.11	2.0
6	2.3	11.6	0.15	2.0
7	2.9	7.6	0.13	2.0
8	2.9	7.6	0.08	2.0
9	2.3	11.9	-0.27	4.0
10	2.3	11.9	-0.19	4.0
11	2.9	7.8	0.00	4.0
12	2.9	7.8	0.80	4.0

### 3.2. Combined Wave Overtopping and Seepage Tests

The setup of the combined wave overtopping and seepage (OS) tests is depicted in Fig. 3-2. The number of tests was 10. The porous layer thickness was 14 cm. The stones were the same for the S and OS tests. The crest width and elevation above the toe of the structure were 55 cm and 30.2 cm, respectively. The crest height above the datum was 9.7 cm. The seaward slope was 1/5. The maximum downward seepage velocity estimated using Eq. (2-14) was 12.8 cm/s. The slope of the beach in front of the structure was the same as that of the S tests. The

offshore boundary conditions of the waves and water level for the OS tests are tabulated in Table 3-3. The spectral peak periods were similar to those for the S tests. The RMS wave heights varied from 7.3 cm to 11.9 cm. The wave set-down or setup and still water level at the offshore boundary were in the range of (-0.89) - 0.37 cm and 0 - 4 cm, respectively.

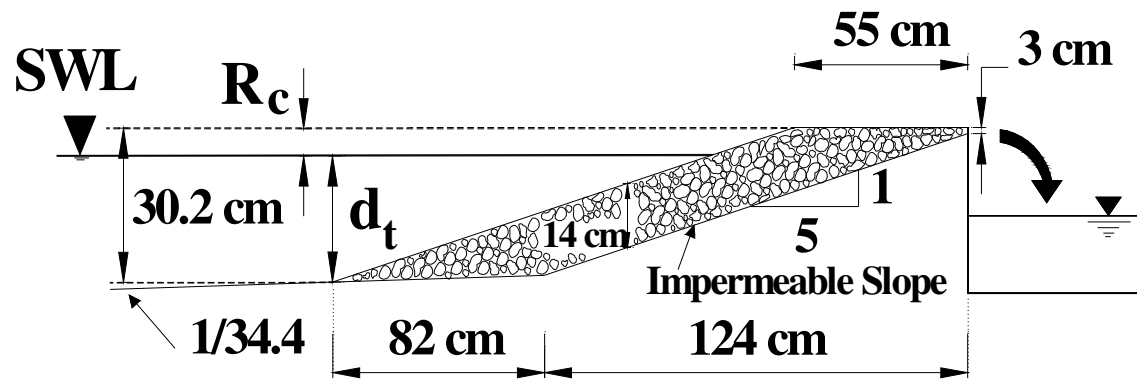


Fig. 3-2. Combined overtopping and seepage (OS) tests with permeable 1/5 slope

**Table 3-3.** Wave Conditions and Still Water Level at  $x = 0$  for Test Series OS

Test No.	$T_p$ (sec)	$H_{rms}$ (cm)	$\bar{\eta}$ (cm)	S (cm)
1	2.3	11.3	0.25	0.00
2	3.0	7.3	0.37	0.00
3	2.3	11.6	-0.10	2.00
4	2.3	11.7	0.12	2.00
5	2.9	7.5	0.06	2.00
6	2.9	7.5	0.06	2.00
7	2.3	11.9	-0.74	4.00
8	2.3	11.9	-0.89	4.00
9	2.9	7.8	-0.30	4.00
10	2.9	7.8	-0.30	4.00

### 3.3. Wave Overtopping Tests

Fig. 3-3 depicts the experimental setup of the wave overtopping (O) tests by Kobayashi and Raichle (1994). The porous layer was a single layer of stones of 4.23 cm nominal diameter. The crest width and its height above the toe of the structure were 18.5 cm and 27.3 cm, respectively. The crest height above the datum was 13 cm. The number of tests was 12. The seaward slope was 1/2. The vertical thickness of the stone layer was 4.73 cm. The porosity of the stone was taken to be the same as that of the S and OS tests. The estimated maximum downward seepage velocity was 14.3 cm/s. The slope of the beach in front of the structure was 1/33. Table 3-4 presents the wave and water level conditions at the offshore boundary of the O

tests. Two different peak periods of 2.0 sec and 2.5 sec were generated. The root mean square wave heights were in the range of 7.4 – 8.5 cm. The wave setup at the offshore boundary was not measured and taken to be zero. The still water level varied from 0.0 to 3.0 cm. During the wave overtopping tests, no seepage occurred.

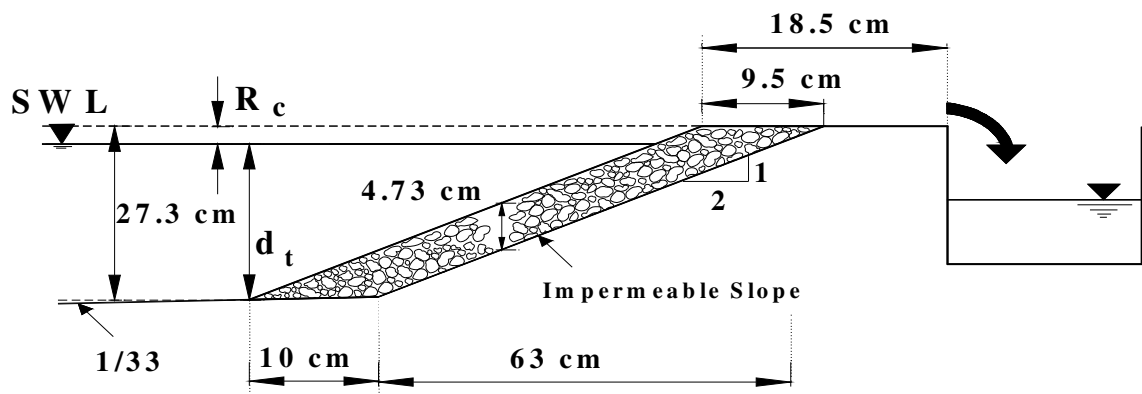


Fig. 3-3. Overtopping (O) tests with permeable 1/2 slope

**Table 3-4.** Wave Conditions and Still Water Level at  $x = 0$  for Test Series O

Test No.	$T_p$ (sec)	$H_{rms}$ (cm)	$\bar{\eta}$ (cm)	S (cm)
1	2.5	7.4	0.0	0.00
2	2.0	7.5	0.0	0.00
3	2.5	7.7	0.0	0.00
4	2.0	8.2	0.0	0.00
5	2.0	7.6	0.0	1.00
6	2.0	8.3	0.0	1.00
7	2.5	7.9	0.0	2.00
8	2.0	7.9	0.0	2.00
9	2.5	8.0	0.0	2.00
10	2.0	8.5	0.0	2.00
11	2.0	7.9	0.0	3.00
12	2.0	8.5	0.0	3.00

### 3.4. Tests by van Gent

Fig. 3-4 shows the experimental setup for the  $D'$  tests by van Gent (2002). The location of  $x = 0$  is taken at the toe of the seaward slope of 1/4 where the incident waves were measured. The crest of 110 cm width was at the height of 60.5 cm and 30.5 cm above the toe of the structure and the datum, respectively. A single layer of gravel with  $D_{n50} = 0.49$  cm was glued on the crest and the landward slope of 1/4 in order to measure the water depth and

velocity above the stationary permeable layer. The stone porosity for the  $D'$  tests was not measured and is assumed to be 0.5 which was the measured value for the S and OS tests.

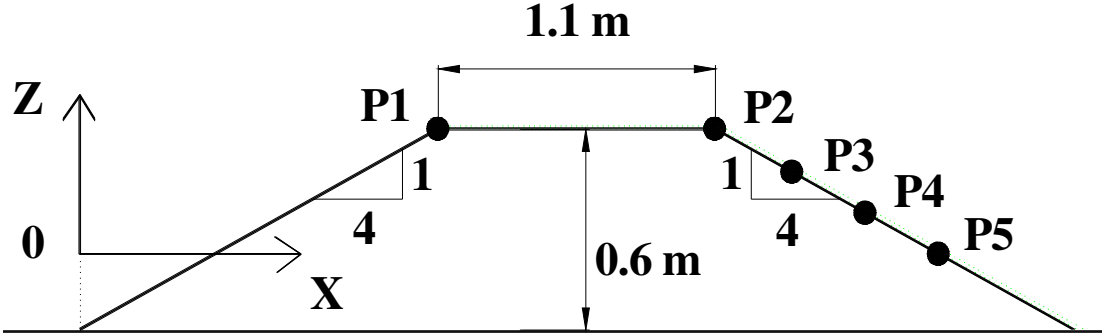


Fig. 3-4.  $D'$  tests conducted by van Gent (2002)

Table 3-5 summarizes the wave and water level conditions at the offshore boundary for the 18 tests by van Gent. The surge  $S$ , RMS wave height and peak period were in the range of 0 - 20 cm, 8.91 - 10.82 cm, 1.58 - 2.51 sec respectively. No wave setup was measured at the seaward boundary where  $\bar{\eta} = 0$  is assumed. For  $D'$  test series the water depth and velocity were measured at five points for each test. Points P1 and P2 were located at the seaward and landward ends of the crest, respectively. Points P3, P4 and P5 were located on the landward slope at elevations of 10, 25 and 40 cm, respectively, below the crest as shown in Fig. 3-4.

**Table 3-5.** Wave Conditions and Still Water Level at  $x = 0$  for Test Series D'

Test No.	$T_P$ (sec)	$H_{rms}$ (cm)	$\bar{\eta}$ (cm)	S (cm)
1	2.51	10.18	0.0	0.00
2	2.02	9.83	0.0	0.00
3	2.50	10.61	0.0	5.00
4	2.00	10.04	0.0	5.00
5	2.49	10.82	0.0	10.00
6	1.99	10.25	0.0	10.00
7	1.59	9.75	0.0	10.00
8	1.98	10.39	0.0	15.00
9	1.59	9.90	0.0	15.00
10	1.59	10.18	0.0	20.00
11	2.50	10.75	0.0	10.00
12	2.50	10.46	0.0	10.00
13	2.45	9.83	0.0	10.00
14	2.45	9.19	0.0	10.00
15	2.00	10.04	0.0	10.00
16	2.00	9.76	0.0	10.00
17	1.60	9.40	0.0	10.00
18	1.58	8.91	0.0	10.00

### 3.5. Model Calibration

The computational input parameters include the constant nodal spacing which is specified to be 1 cm. The breaker ratio parameter  $\gamma$  involved in the estimation of the wave energy dissipation rate due to wave breaking in the wet zone was taken in the range of 0.7 to 0.9 by Kobayashi and de los Santos (2007). The comparisons of the computed and measured overtopping rates for the 52 tests based on  $\gamma = 0.7, 0.8$  and  $0.9$  are shown in Fig. 3-5 where use is made of the parameter  $\alpha_m$  calibrated below. The solid and dashed lines in this and subsequent figures indicate the perfect agreement and deviation of a factor of 2, respectively. The overall agreement for  $q_o$  is slightly better for  $\gamma = 0.8$  which is adopted for the subsequent computations. The bottom friction factor  $f_b$  for the smooth impermeable bottom is taken as  $f_b = 0.002$  calibrated by Kobayashi et al. (2010) using 207 tests for wave overtopping of smooth impermeable structures. For the rough permeable bottom, use is made of  $f_b = 0.01$  calibrated by Kobayashi and de los Santos (2007) for their wet zone model.

The empirical parameter  $\alpha_m$  introduced in Eq. (2-12) is calibrated using the 52 tests. Initially, the downward momentum flux was neglected in Eq. (2-2), corresponding to  $\alpha_m = 0$  in the present numerical model. The computed wave overtopping rates for  $\alpha_m = 0$  were too large by one order of magnitude. In addition, the model overpredicted the wave overtopping probabilities. Figs. 3-6 and 3-7 depict the comparisons of the measured and computed wave overtopping rates and probabilities based on  $\alpha_m = 0$ . In Fig. 3-6, the agreement is better for O and D' test series with the single layer of the stone. The numerical model clearly overpredicts the wave overtopping rates for S and OS tests series because the permeable layer is the four

layers of the stone in those tests series. Therefore, the downward momentum flux due to the flow infiltration should reduce the wave overtopping rate in S and OS test series.

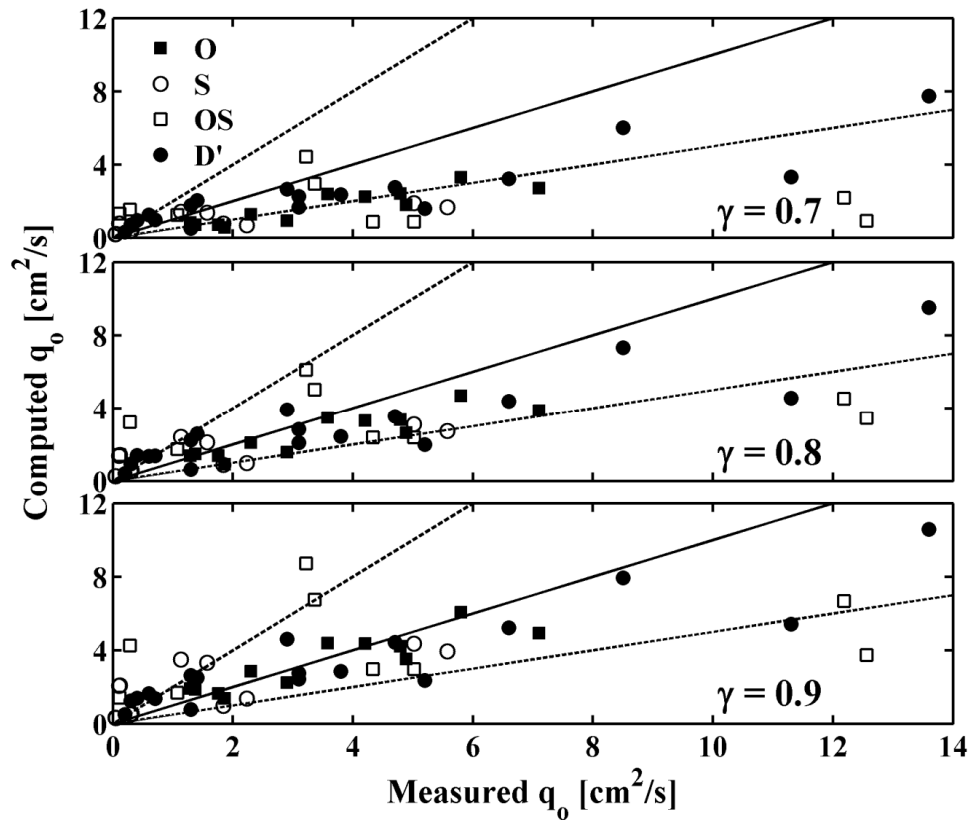


Fig. 3-5. Comparison of measured and computed wave overtopping rates for  $\gamma = 0.7, 0.8$  and 0.9

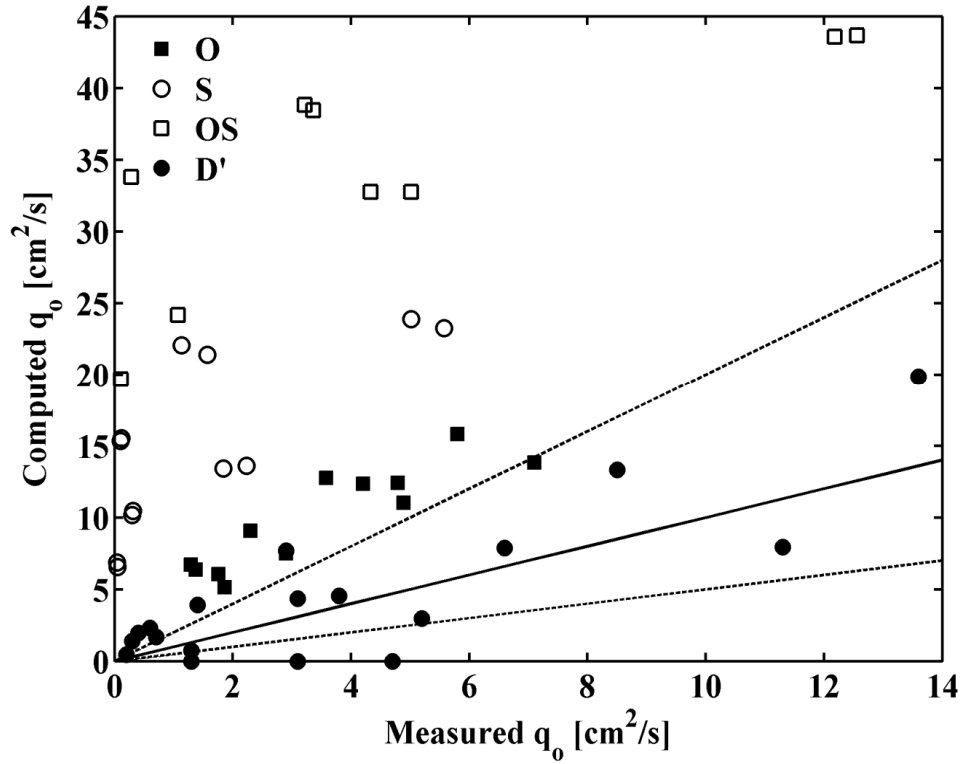


Fig. 3-6. Comparison of measured and computed wave overtopping rates for  $\alpha_m = 0$

Fig. 3-7, shows the comparison of the measured and computed wave overtopping probabilities for O and D' test series. The wave overtopping probability was not measured for S and OS test series. The probability of wave overtopping is overpredicted if  $\alpha_m = 0$  except for 4 tests.

In order to eradicate this shortcoming, Eq. (2-12) has been introduced to account for the vertical momentum flux in the momentum equation. The empirical formula for the parameter  $\alpha_m$  in Eq. (2-12) developed using the present 52 tests is expressed as

$$\alpha_m = \alpha \left( \frac{h_p}{D_{n50}} \right)^\mu \quad (3-1)$$

where  $h_p = (z_b - z_p)$  = local permeable layer thickness (see Fig. 2-2). The parameters  $\alpha$  has been calibrated for the range of 0.3 - 3 but is taken as  $\alpha = 2$  in Eq. (2-18) to reduce the number of the empirical parameters. The comparisons of the measured and computed overtopping rates for  $\mu = 0.1, 0.3$  and  $1.0$  in Eq. (3-1) are shown in Fig. 3-8 which indicates  $\mu = 0.3$  for the present 52 tests. In Eq. (3-1),  $h_p/D_{n50}$  is the local thickness of the permeable layer normalized by the nominal stone diameter. This thickness correction reduces the computed  $q_o$  for S and OS test series with  $t_a/D_{n50} = 4.1$  in Table 1. For O and D' test series,  $\alpha_m \simeq \alpha$  on the permeable layer. Eq. (3-1) ensures  $\alpha_m = 0$  in the zone of  $z_b = z_p$  and no permeable layer.

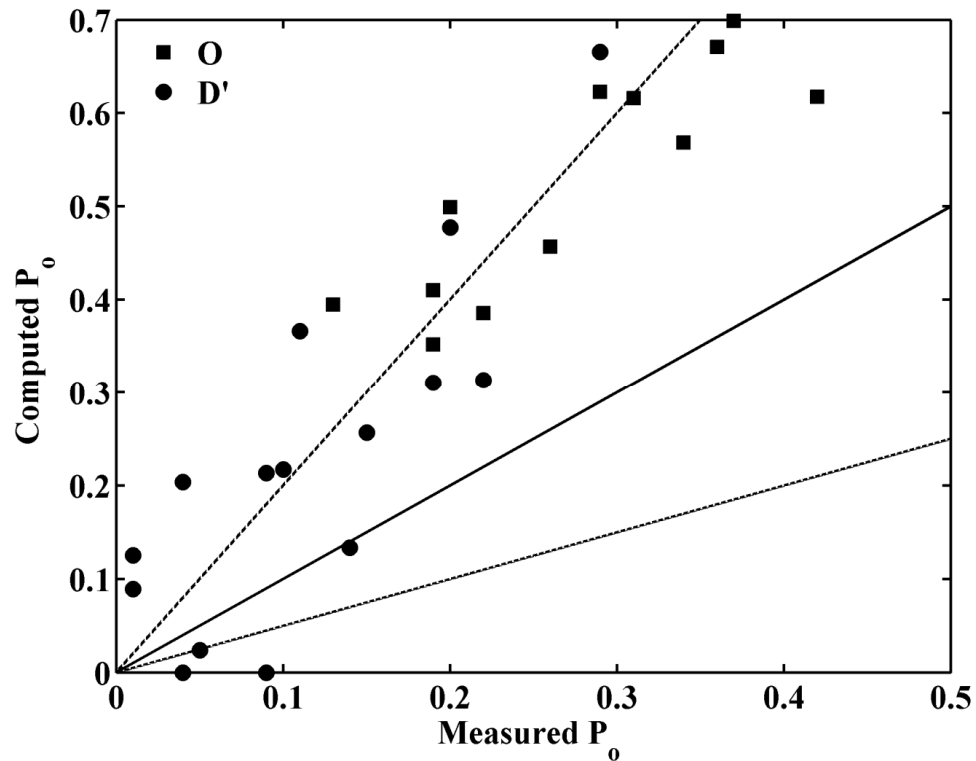


Fig. 3-7. Comparison of measured and computed wave overtopping probabilities for  $\alpha_m = 0$

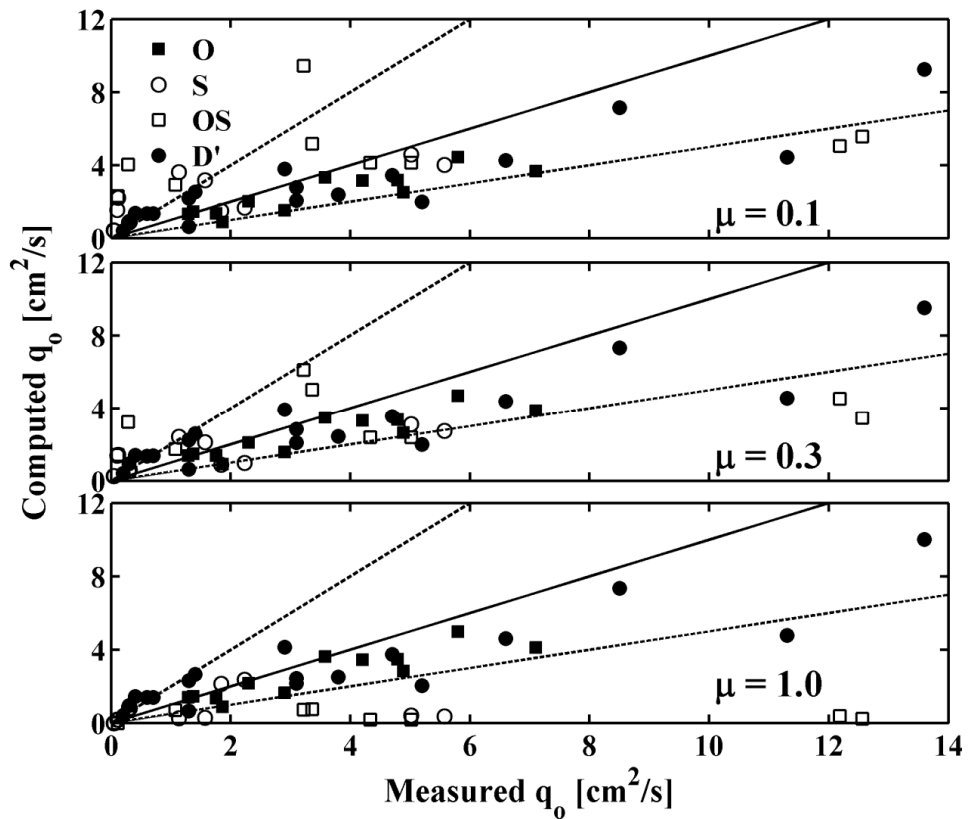


Fig. 3-8. Comparison of measured and computed wave overtopping rates for  $\mu = 0.1, 0.3$  and 1

### 3.6. Comparison of Calibrated Model with Data

Fig. 3-9 compares the measured and computed wave overtopping rates for O, S, OS and D' test series. Most of the data points fall within the deviation of the factor of 2. The wave overtopping probability was measured for O and D' test series. Fig. 3-10 compares the measured and computed probabilities for these test series. The agreement is mostly within the

factor of about 2. Table 3-6 to Table 3-9 list the values used to plot Figs 3-9 and 3-10 for the four tests series.

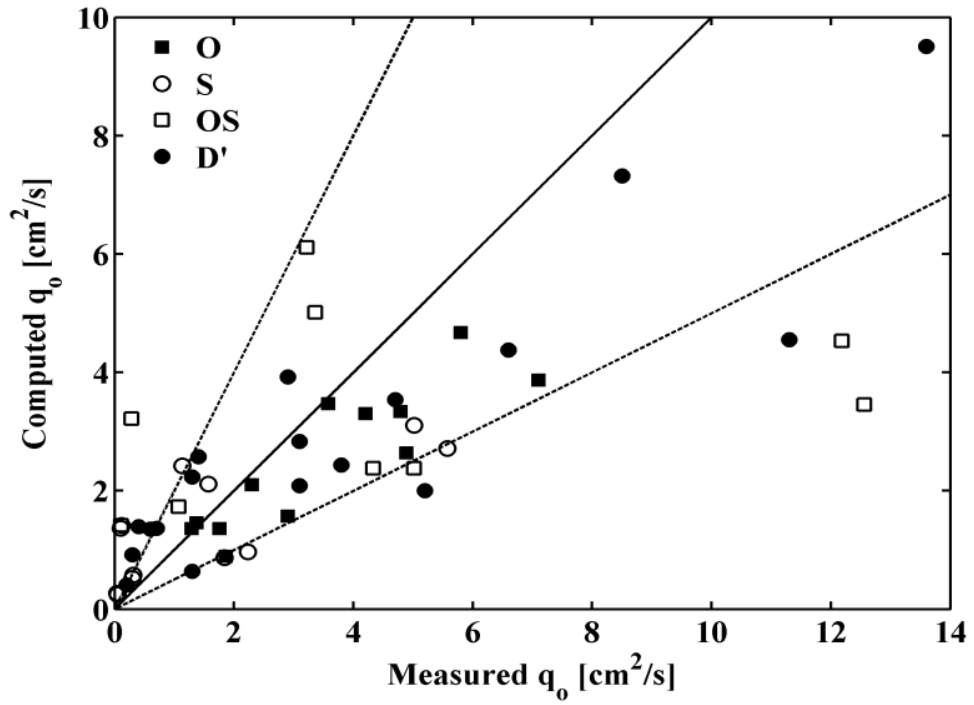


Fig. 3-9. Comparison of measured and computed wave overtopping rates

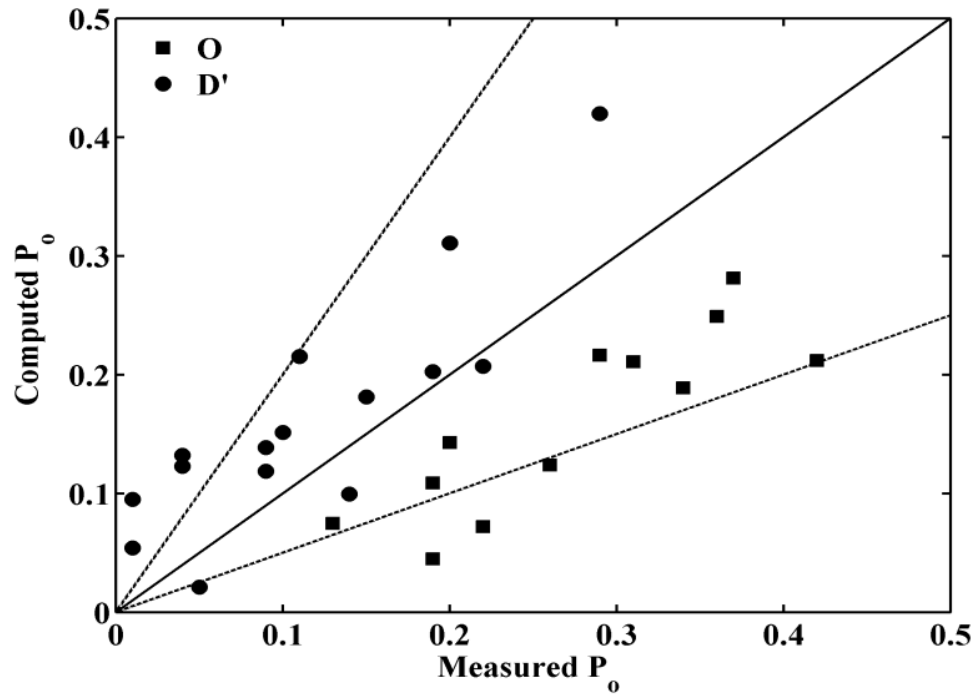


Fig. 3-10. Comparison of measured and computed wave overtopping probabilities

**Table 3-6.** Measured and Computed Wave Overtopping Probabilities and Rates for D' Test Series

Test No.	Computed	Measured	Computed	Measured
	$P_o$	$P_o$	$q_o$ (cm <sup>2</sup> /sec)	$q_o$ (cm <sup>2</sup> /sec)
1	0.02	0.05	0.64	1.30
2	0.02	NM	0.41	0.20
3	0.10	0.14	2.0	5.20
4	0.05	0.01	1.37	0.70
5	0.21	0.22	4.55	11.30
6	0.14	0.09	2.83	3.10
7	0.09	0.01	1.35	0.60
8	0.31	0.20	7.32	8.50
9	0.21	0.11	3.92	2.90
10	0.42	0.29	9.51	13.60
11	0.20	0.19	4.38	6.60
12	0.18	0.15	3.54	4.70
13	0.15	0.10	2.43	3.80
14	0.12	0.09	2.09	3.10
15	0.13	0.04	2.57	1.40
16	0.12	0.04	2.23	1.30
17	0.06	NM	1.40	0.40
18	0.04	NM	0.92	0.30

**Table 3-7.** Computed Wave Overtopping Probability and Measured and Computed Rates for  
S Test Series

Test No.	Computed	Computed	Measured
	$P_o$	$q_o$ (cm <sup>2</sup> /sec)	$q_o$ (cm <sup>2</sup> /sec)
1	0.07	1.41	0.12
2	0.07	1.36	0.10
3	0.01	0.27	0.04
4	0.01	0.25	0.05
5	0.09	2.11	1.57
6	0.10	2.42	1.13
7	0.02	0.57	0.31
8	0.02	0.52	0.30
9	0.12	2.72	5.57
10	0.13	3.11	5.02
11	0.03	0.97	2.23
12	0.03	0.87	1.84

**Table 3-8.** Computed Wave Overtopping Probability and Measured and Computed Rates for OS Test Series

Test No.	Computed	Computed	Measured
	$P_o$	$q_o$ (cm <sup>2</sup> /sec)	$q_o$ (cm <sup>2</sup> /sec)
1	0.15	3.22	0.28
2	0.09	1.41	0.11
3	0.21	5.02	3.36
4	0.24	6.11	3.22
5	0.11	1.73	1.07
6	0.11	1.73	1.07
7	0.22	4.53	12.18
8	0.19	3.45	12.56
9	1.0	2.38	4.33
10	1.0	2.38	5.02

**Table 3-9.** Measured and Computed Wave Overtopping Probabilities and Rates for O Test Series

Test No.	Computed	Measured	Computed	Measured
	$P_o$	$P_o$	$q_o$ (cm <sup>2</sup> /sec)	$q_o$ (cm <sup>2</sup> /sec)
1	0.07	0.22	1.36	1.76
2	0.05	0.19	0.89	1.86
3	0.11	0.19	1.36	1.29
4	0.08	0.13	1.46	1.37
5	0.12	0.26	1.57	2.90
6	0.14	0.20	2.10	2.30
7	0.21	0.42	3.33	4.79
8	0.19	0.34	2.64	4.89
9	0.22	0.29	3.47	3.58
10	0.21	0.31	3.30	4.20
11	0.25	0.36	3.87	7.10
12	0.28	0.37	4.67	5.80

As mentioned earlier in Section 3.4, van Gent (2002) measured the water depth and velocity at five different locations on the crest and landward slope of the structure. The measured water depth and velocity at P1, P2, P3, P4 and P5 were analyzed on the basis of individual wave overtopping events. The values tabulated in his report are the water depth  $h_{2\%}$ , velocity  $U_{2\%}$ , and discharge  $q_{2\%}$  corresponding to the values exceeded by 2% of the incident

1,000 waves. It is noted that the numerical model is based on the vertical depth  $h$  and the horizontal velocity  $U$ . The measured depth was the depth normal to the slope and the measured velocity was parallel to the slope. The differences of  $h$  and  $U$  defined differently are 3% on the slope of 1/4 and neglected in the following comparisons.

Before the comparison with the measured 2% values, the computed hydrodynamic variables are examined using D'5 and D'10 tests (the 5-th and 10-th conditions in Table 3-5). Fig. 3-11 and 3-12 show the computed cross-shore variations. The peak wave periods of D'5 and D'10 tests were 2.49 sec and 1.59 sec, respectively. The mean water level  $(\bar{\eta} + S)$  above  $z = 0$  and the bottom elevation are plotted together in the top panel of Figs. 3-11 and 3-12. The free surface standard deviation  $\sigma_{\eta}$ , mean velocity  $\bar{U}$ , and velocity standard deviation  $\sigma_U$  are plotted in the middle three panels. The wet probability  $P_w$  is shown in the bottom panel where  $P_w = 1$  in the wet zone. The still water depths at the toe of the 1/4 slope for tests D'5 and D'10 were 40 cm and 50 cm, respectively. The computed mean depth  $\bar{h} = (\bar{\eta} + S - z_b)$  is of the order of 1 cm or less in the wet and dry zone. The RMS wave heights for tests D'5 and D'10 at the offshore boundary  $x = 0$  were 10.82 cm and 10.18 cm, respectively. The standard deviation  $\sigma_{\eta}$  related to the RMS wave height by  $H_{rms} = \sqrt{8}\sigma_{\eta}$  gradually increases due to shoaling and then decreases rapidly because the incident waves break as  $\bar{h}$  decreases. The standard deviation  $\sigma_{\eta}$  reduces to the order of a few millimeters at the end of the computational domain. The mean velocity  $\bar{U}$  is negative (offshore) near the still water shoreline due to the return flow on the seaward slope. The mean velocity becomes positive (onshore) on the landward slope where the landward velocity is as large as 9 cm/s and 17 cm/s due to the

computed wave overtopping rates of  $q_o = 4.55 \text{ cm}^2/\text{s}$  and  $9.51 \text{ cm}^2/\text{s}$  for D'5 and D'10 tests, respectively. The velocity standard deviation  $\sigma_U$  peaks near the still water shoreline, decreases toward the crest and increases on the landward slope to become as large as 49 cm/s and 62 cm/s for D'5 and D'10 tests, respectively. The wet probability decreases rapidly on the seaward slope and decreases gradually on the crest and landward slope.

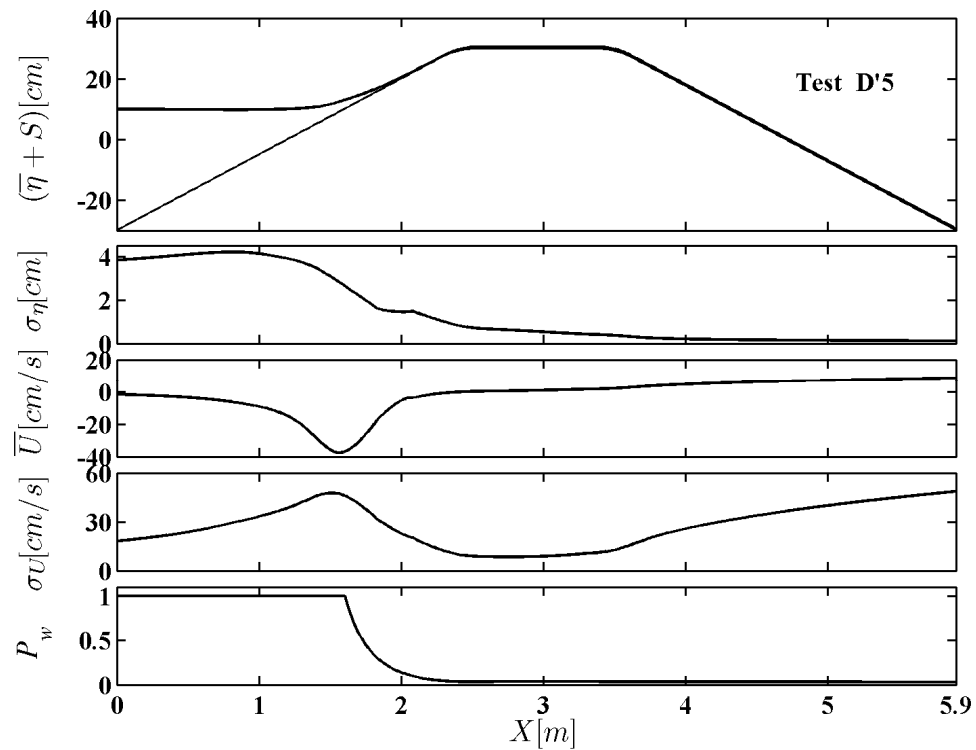


Fig. 3-11. Spatial variations of mean water level, free surface standard deviation, mean velocity, velocity standard deviation and wet probability for D'5 test

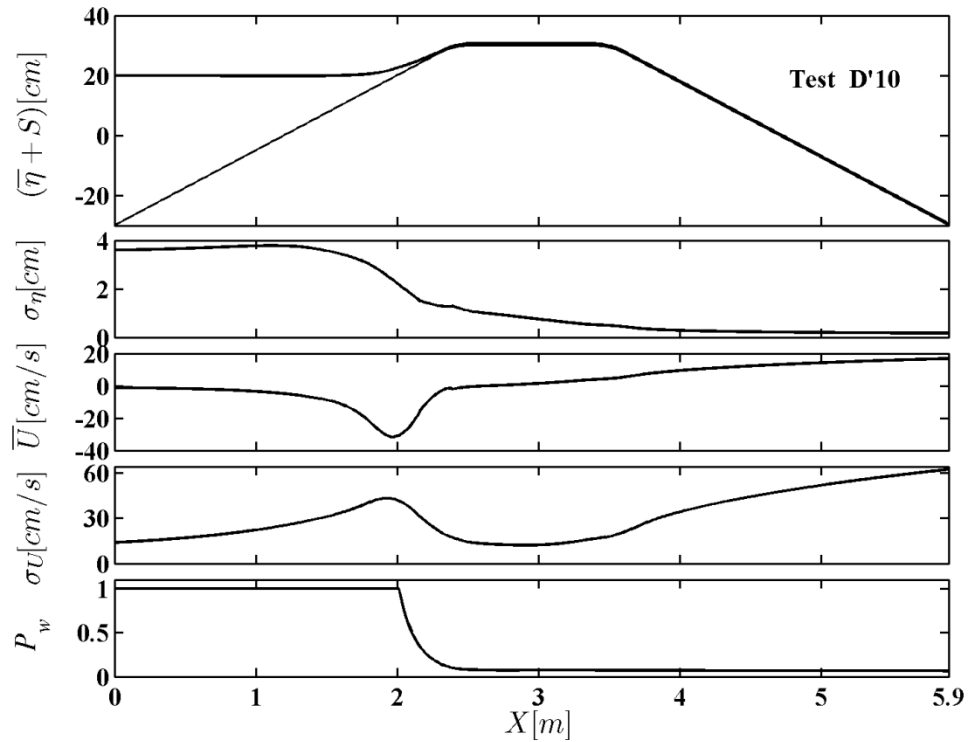


Fig. 3-12. Spatial variations of mean water level, free surface standard deviation, mean velocity, velocity standard deviation and wet probability for D'10 test

As for the other tests series, Figs. 3-13, 3-14 and 3-15 show the computed cross-shore variations for tests S11, OS3 and O9, respectively. The cross-shore variations on the beach are relatively small. The variations on the seaward slope and crest of the structure are qualitatively similar to those shown in Figs. 3-11 and 3-12. It is noted that a kink in the cross-shore variations occurs sometimes in the transition zone (Fig. 2-1) between the wet model and the wet and dry model which are two different models. The input bottom geometry is smoothed to reduce the sudden change of the bottom slope and possible numerical fluctuations.

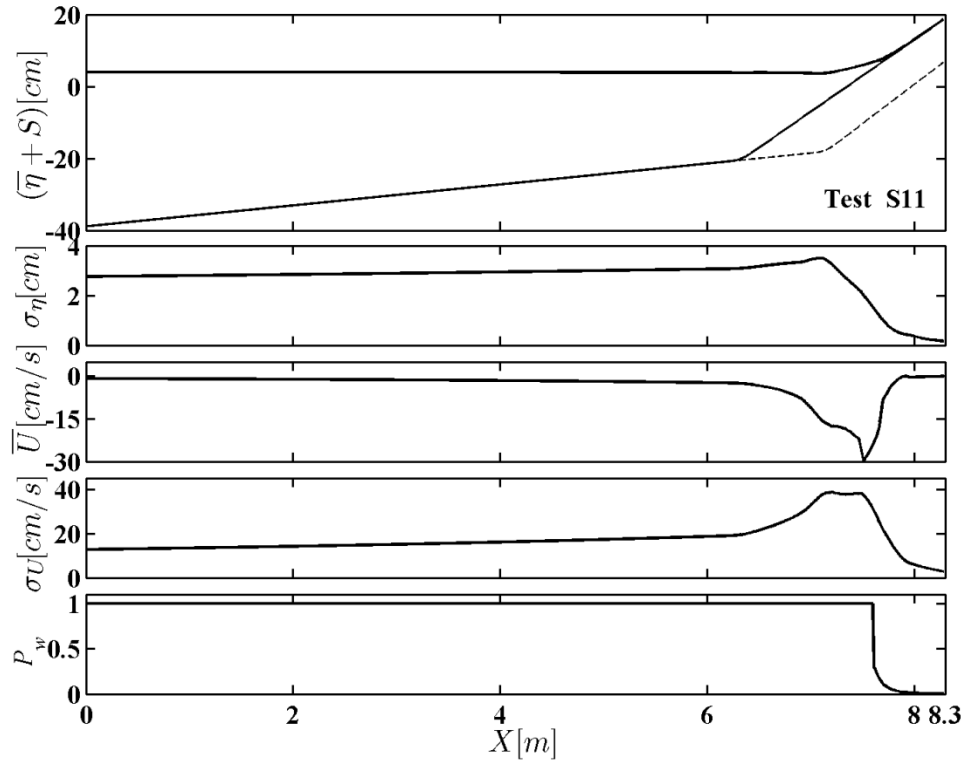


Fig. 3-13. Spatial variations of mean water level, free surface standard deviation, mean velocity, velocity standard deviation and wet probability for S11 test

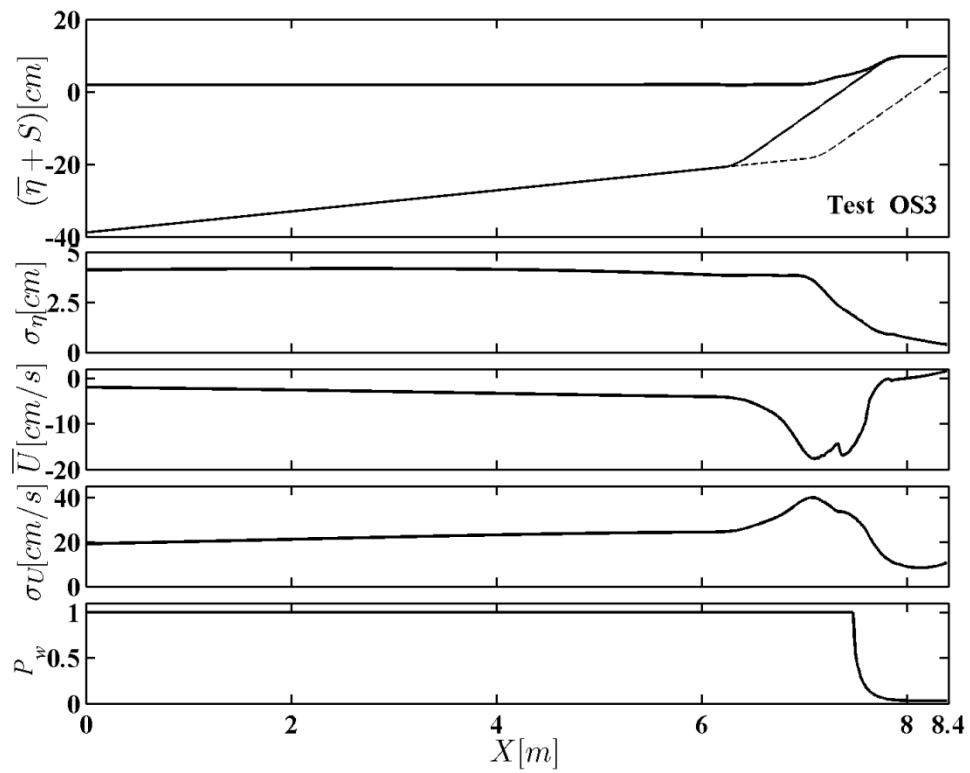


Fig. 3-14. Spatial variations of mean water level, free surface standard deviation, mean velocity, velocity standard deviation and wet probability for OS3 test

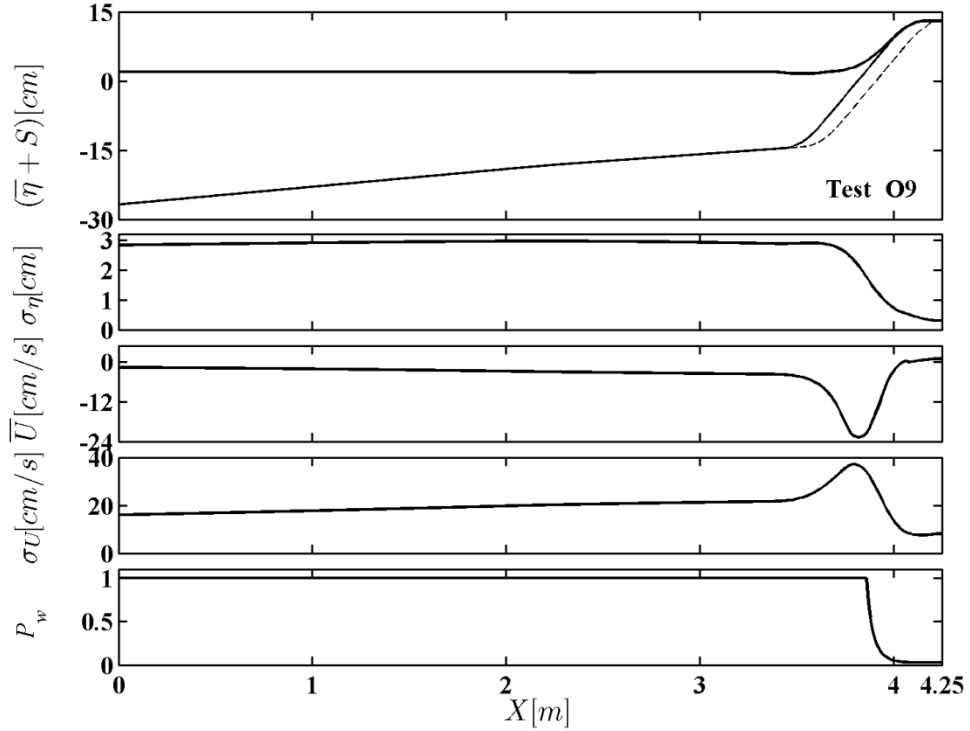


Fig. 3-15. Spatial variations of mean water level, free surface standard deviation, mean velocity, velocity standard deviation and wet probability for O9 test

For the comparison of the measured 2% values by van Gent (2002), the exceedance probability is considered. For the probability density function  $f(h)$  given by Eq. (2-15), the water depth  $h_e$  corresponding to the exceedance probability  $e$  is given by

$$h_e = \frac{\bar{h}}{P_w} \ln\left(\frac{P_w}{e}\right) \quad \text{for } P_w > e \quad (3-2)$$

Using Eq. (2-18), the water velocity  $U_e$  and discharge  $q_e$  corresponding to the exceedance probability  $e$  are expressed as

$$U_e = \alpha \sqrt{gh_e} + U_s \quad ; \quad q_e = h_e U_e \quad (3-3)$$

The probability  $e$  of  $h > h_e$  at given  $x$  is not directly related to the probability based on individual overtopping events. The probability 2% used by van Gent (2002) is assumed to correspond to the range of  $e = 0.01 - 0.02$  where Eq. (3-2) is not very sensitive to  $e = 0.01 - 0.02$  as long as the wet probability  $P_w$  is larger than about 0.1. The computed values of  $h_e, U_e$  and  $q_e$  presented in the following are based on  $e = 0.01$  where use is made of  $e = P_w / 1.1$  if  $P_w < 0.011$  so that  $(P_w / e) \geq 1.1$  in Eq. (3-2).

Figs. 3-16 and 3-17 compare the measured and computed cross-shore variations of  $h_{2\%}$ ,  $U_{2\%}$  and  $q_{2\%}$  for tests D'5 and D'10 where  $x_{SWL} = 1.6$  m and  $x_{SWL} = 2$  m are the seaward limit of the wet and dry zone for tests D'5 and D'10, respectively. The agreement is within the factor of 2. The water depth  $h_{2\%}$  decreases landward and becomes very small in both tests. The corresponding velocity  $U_{2\%}$  decreases on the seaward slope and crest and increases downward on the landward slope where the crest is located in the zone of  $x = 2.4 - 3.5$  m. The cross-shore variation of  $q_{2\%}$  is similar to that of  $h_{2\%}$  because  $U_{2\%}$  varies much less than  $h_{2\%}$ .

Fig. 3-18, compares the measured and computed values of  $h_{2\%}$  at the five points P1 to P5 (see Fig. 3-4) for D' test series. The numerical model tends to overpredict  $h_{2\%}$  at P1 probably

because of the sudden change in bed roughness and porosity but in general the agreement is mostly within the factor of 2.

Fig. 3-19 shows the comparison of the measured and computed values of  $U_{2\%}$  at the five points. The numerical model does not predict  $U_{2\%}$  at P4 and P5 well. However, most of the data points fall within the factor of 2.

Fig. 3-20 depicts the comparison of the measured and computed wave overtopping of  $q_{2\%}$  at the five points. The numerical model overestimates  $q_{2\%}$  at P1. The agreement is mostly within the factor of 2. It should be mentioned that the hydrodynamic variables in the wet and dry zone are difficult to predict accurately due to the small water depth and larger velocity during intermittent wave overtopping.

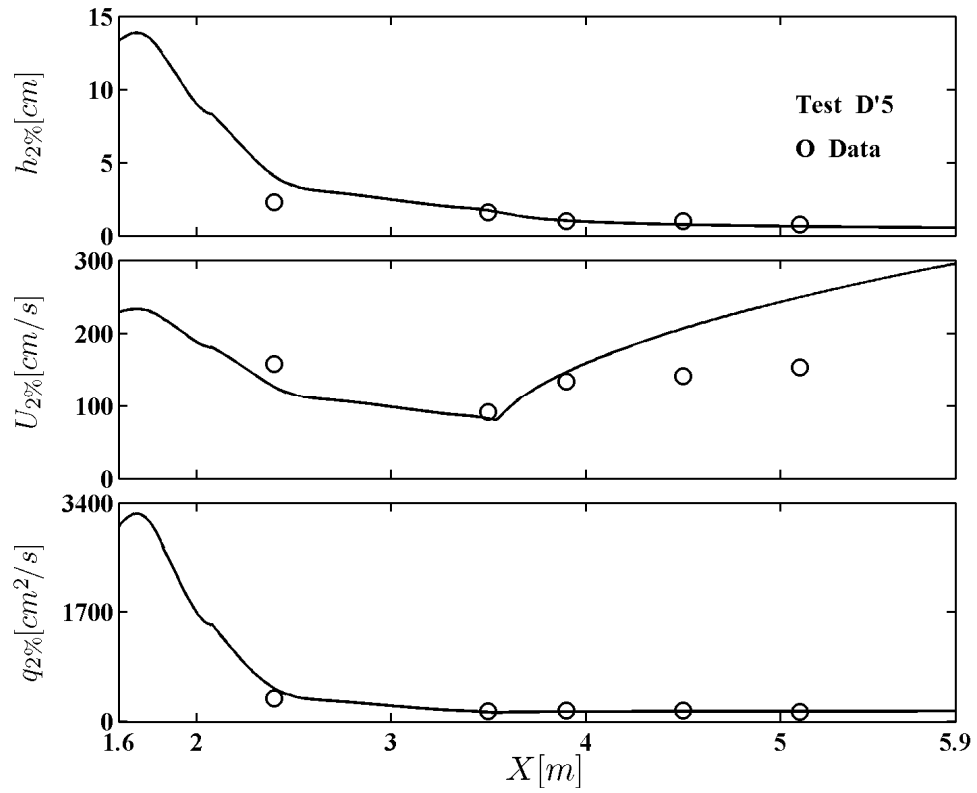


Fig. 3-16. Comparison of measured and computed cross-shore variations of  $h_{2\%}$ ,  $U_{2\%}$  and  $q_{2\%}$  for D'5 test

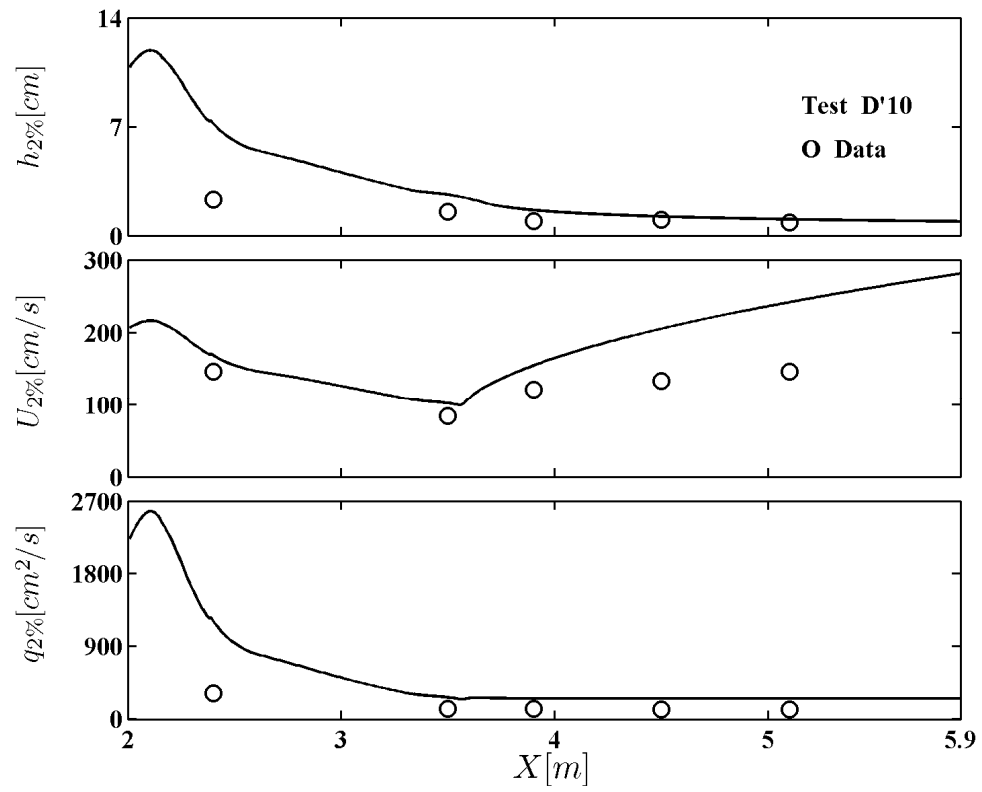


Fig. 3-17. Comparison of measured and computed cross-shore variations of  $h_{2\%}$ ,  $U_{2\%}$  and  $q_{2\%}$  for D'10 test

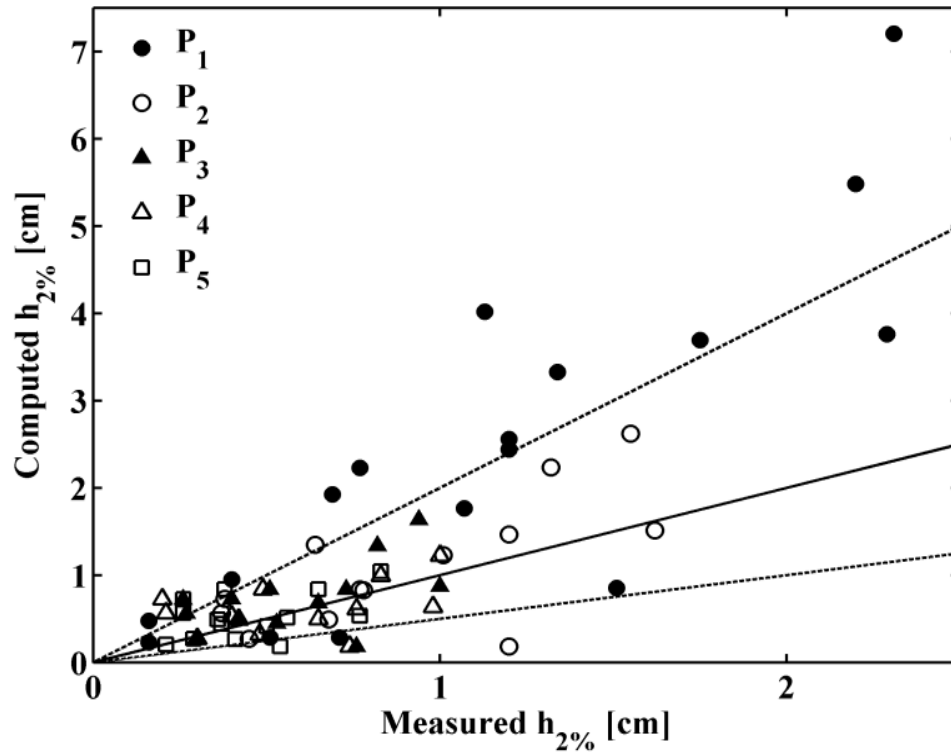


Fig. 3-18. Comparison of measured and computed values of  $h_{2\%}$  for D' test series

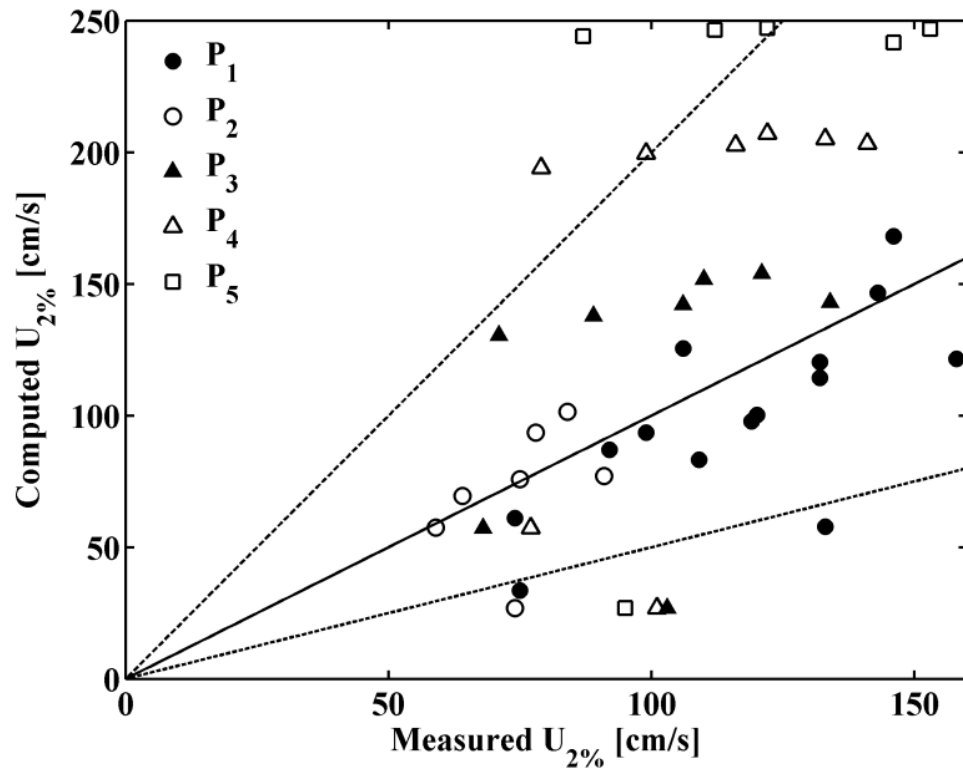


Fig. 3-19. Comparison of measured and computed values of  $U_{2\%}$  for D' test series

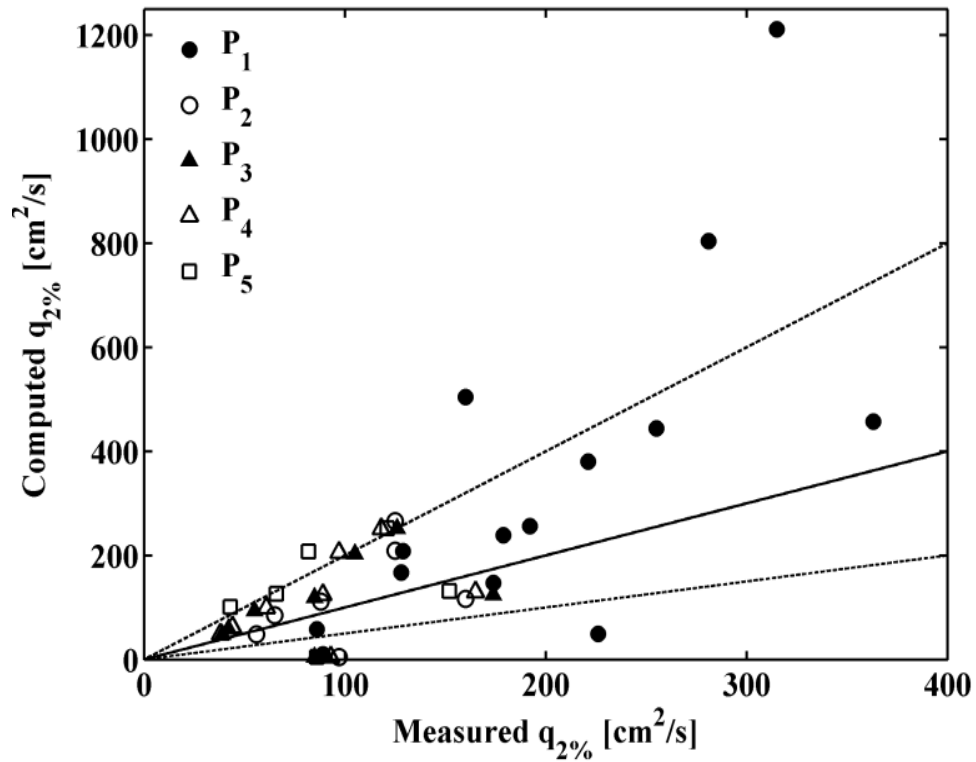


Fig. 3-20. Comparison of measured and computed values of  $q_{2\%}$  for D' test series

### 3.7. Permeability Effects

In order to assess the permeability effects on the computed results, the numerical model was run for each test series with and without permeability. The computational parameters are kept the same. The option IPERM=1 for the numerical model CSHORE includes a permeable layer, while the option of IPERM=0 regards the bottom impermeable.

Figs. 3-21 – 3-22 show the comparisons for the wave overtopping rates for all tests series and for the wave overtopping probabilities for O and D' test series for IPERM=0. The

computed wave overtopping rates are significantly overestimated for S and OS test series with the thicker permeable layers. The wave overtopping rates for D' test series are predicted within a factor of two because of the single layer of glued gravel. The wave overtopping probabilities of O and D' tests series are overpredicted by a factor of 2 in Fig. 3-22.

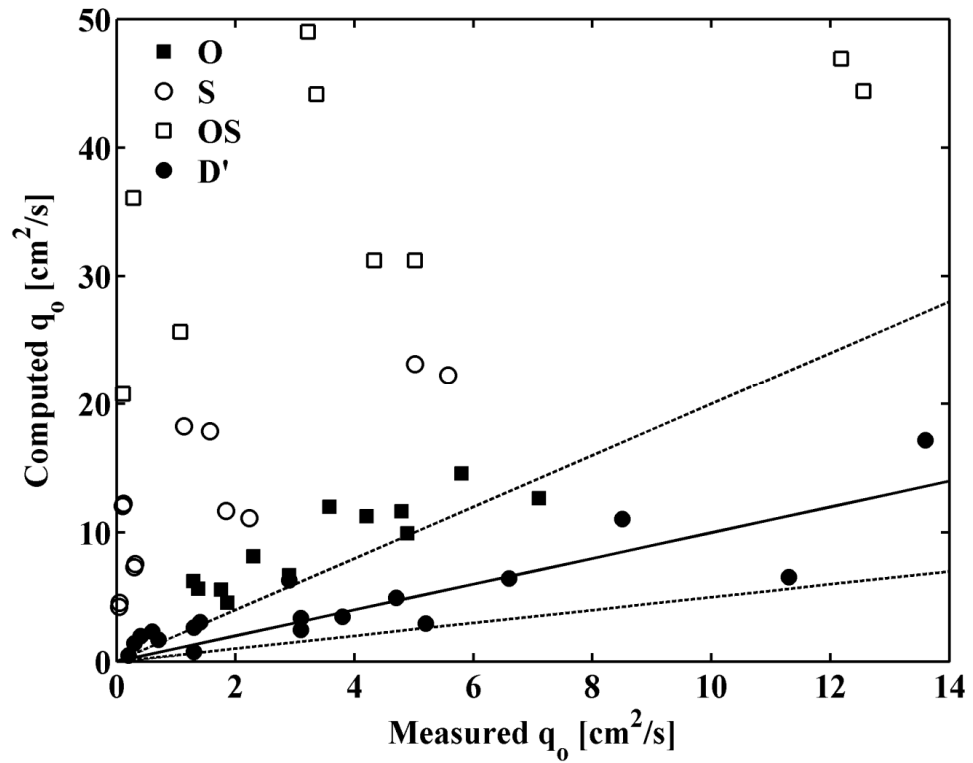


Fig. 3-21. Comparison of measured and computed wave overtopping rates for IPERM=0

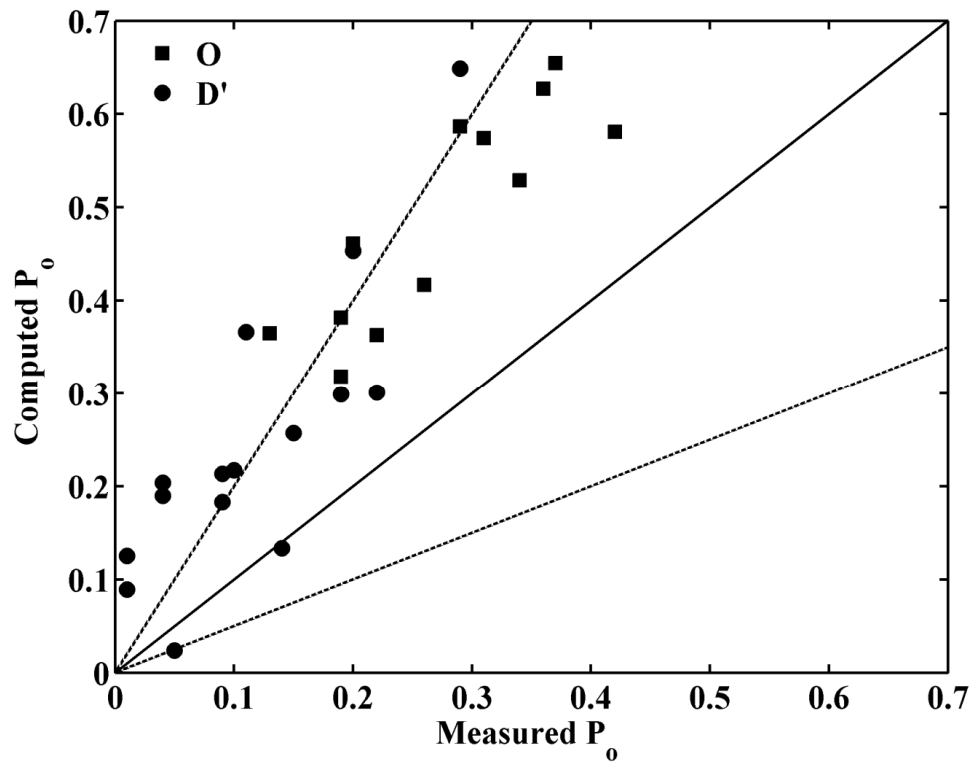


Fig. 3-22. Comparison of measured and computed wave overtopping probabilities for IPERM=0

Comparing Figs. 3-6 and 3-21 and Figs. 3-7 and 3-22, the difference between  $\alpha_m = 0$  in Eq.(2-12) and IPERM=0 can be discerned where the case of  $\alpha_m = 0$  neglects the momentum flux into the permeable layer but includes the volume flux  $q_p$  inside the permeable layer in Eq.(2-6). These figures show the importance of both momentum and volume fluxes in the permeable layer especially if the permeable layer is thick.

Table 3-10 to Table 3-13 summarize the computed wave overtopping rates and probabilities for the four tests series for IPERM=0 and 1.

**Table 3-10.** Computed Wave Overtopping Probability and Rate with IPERM=0 and 1 for D'

Test Series

Test No.	IPERM=1	IPERM=0	IPERM=1	IPERM=0
	P <sub>o</sub>	P <sub>o</sub>	q <sub>o</sub> (cm <sup>2</sup> /sec)	q <sub>o</sub> (cm <sup>2</sup> /sec)
1	0.02	0.02	0.64	0.74
2	0.02	0.02	0.41	0.47
3	0.10	0.13	2.0	2.96
4	0.05	0.09	1.37	1.70
5	0.21	0.30	4.55	6.54
6	0.14	0.21	2.83	3.36
7	0.09	0.13	1.35	2.32
8	0.31	0.45	7.32	11.07
9	0.21	0.37	3.92	6.30
10	0.42	0.65	9.51	17.17
11	0.20	0.30	4.38	6.46
12	0.18	0.26	3.54	4.95
13	0.15	0.22	2.43	3.49
14	0.12	0.18	2.09	2.46
15	0.13	0.20	2.57	3.05
16	0.12	0.19	2.23	2.64
17	0.06	0.11	1.40	1.96
18	0.04	0.10	0.92	1.40

**Table 3-11.** Computed Wave Overtopping Probability and Rate with IPERM=0 and 1 for S

Test Series

Test No.	IPERM=1	IPERM=0	IPERM=1	IPERM=0
	P <sub>o</sub>	P <sub>o</sub>	q <sub>o</sub> (cm <sup>2</sup> /sec)	q <sub>o</sub> (cm <sup>2</sup> /sec)
1	0.07	0.44	1.41	12.23
2	0.07	0.44	1.36	12.07
3	0.01	0.24	0.27	4.26
4	0.01	0.25	0.25	4.55
5	0.09	0.54	2.11	17.87
6	0.10	0.55	2.42	18.26
7	0.02	0.37	0.57	7.58
8	0.02	0.36	0.52	7.31
9	0.12	0.63	2.72	22.29
10	0.13	0.63	3.11	23.16
11	0.03	0.49	0.97	11.14
12	0.03	0.50	0.87	11.69

**Table 3-12.** Computed Wave Overtopping Probability and Rate with IPERM=0 and 1 for OS

Test Series

Test No.	IPERM=1	IPERM=0	IPERM=1	IPERM=0
	$P_o$	$P_o$	$q_o$ (cm <sup>2</sup> /sec)	$q_o$ (cm <sup>2</sup> /sec)
1	0.15	0.80	3.22	36.06
2	0.09	0.70	1.41	20.76
3	0.21	0.88	5.02	44.16
4	0.24	0.89	6.11	48.99
5	0.11	0.80	1.73	25.65
6	0.11	0.80	1.73	25.65
7	0.22	0.93	4.53	46.92
8	0.19	0.93	3.45	44.39
9	1.0	0.90	2.38	31.24
10	1.0	0.90	2.38	31.24

**Table 3-13.** Computed Wave Overtopping Probability and Rate with IPERM=0 and 1 for O  
Test Series

Test No.	IPERM=1	IPERM=0	IPERM=1	IPERM=0
	$P_o$	$P_o$	$q_o$ (cm <sup>2</sup> /sec)	$q_o$ (cm <sup>2</sup> /sec)
1	0.07	0.36	1.36	5.57
2	0.05	0.32	0.89	4.56
3	0.11	0.38	1.36	6.23
4	0.08	0.36	1.46	5.63
5	0.12	0.42	1.57	6.70
6	0.14	0.46	2.10	8.16
7	0.21	0.58	3.33	11.66
8	0.19	0.53	2.64	9.95
9	0.22	0.59	3.47	11.99
10	0.21	0.57	3.30	11.26
11	0.25	0.63	3.87	12.66
12	0.28	0.65	4.67	14.58

Fig. 3-23 shows the comparison of the computed results of D/5 for IPERM=0 and 1. The mean water level plotted in the top panel is affected little by the permeable bottom. In the second panel, the free surface standard deviation indicates no major difference due to the single gravel layer. The cross-shore mean velocity is plotted in the third panel. The velocity variation is identical up to the seaward end of the crest but the difference becomes discernible

on the crest and landward slope with the glued gravel layer. The velocity difference becomes as large as 10 cm/sec at the landward end of the computational domain. The velocity standard deviation is larger on the impermeable crest and landward slope where the difference in  $\sigma_U$  reaches up to 20 cm/sec. The wet probability is larger on the impermeable bottom on the crest and landward slope as expected physically. The comparison for D'10 test shown in Fig. 3-24 is similar because the single gravel layer glued on the crest and landward slope was the same for D' test series.

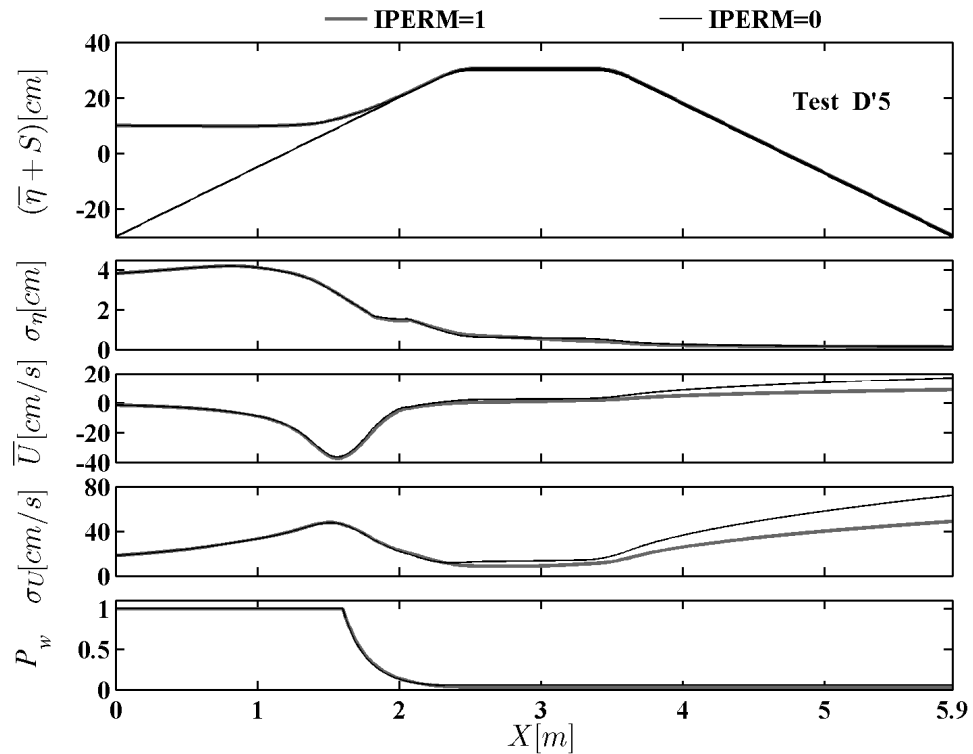


Fig. 3-23. Comparison of mean water level, free surface standard deviation, mean velocity, velocity standard deviation and wet probability for permeable and impermeable bottoms for D'5 test

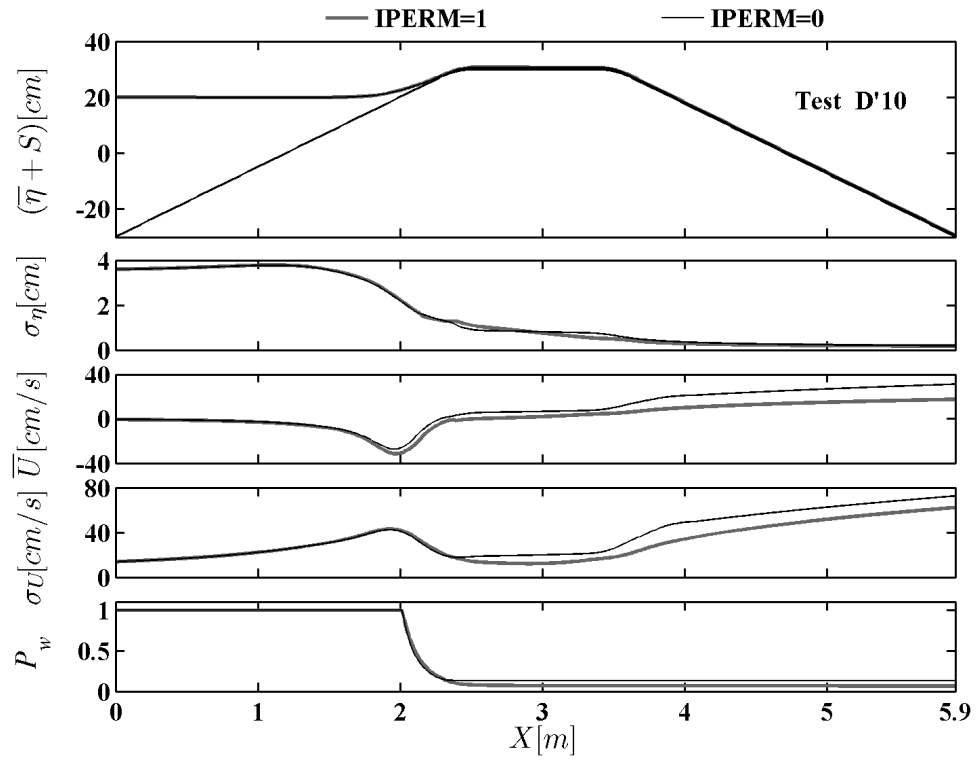


Fig. 3-24. Comparison of mean water level, free surface standard deviation, mean velocity, velocity standard deviation and wet probability for permeable and impermeable bottoms for D'10 test

Fig. 3-25 shows the cross-shore variations of the same hydrodynamic variables for S11 test with IPERM=0 and 1. The mean water level is similar for the two bottom conditions. The free surface standard deviation is larger for the impermeable bottom landward of the still water shoreline. The mean velocity profile is similar up to the still water shoreline. The mean velocity increases landward and becomes as large as 5 cm/sec for IPERM=0 whereas the mean velocity is almost zero for the permeable bottom. The velocity standard deviation is larger for

IPERM=0 above the still water shoreline. The wet probability is larger above the still water shoreline for IPERM=0.

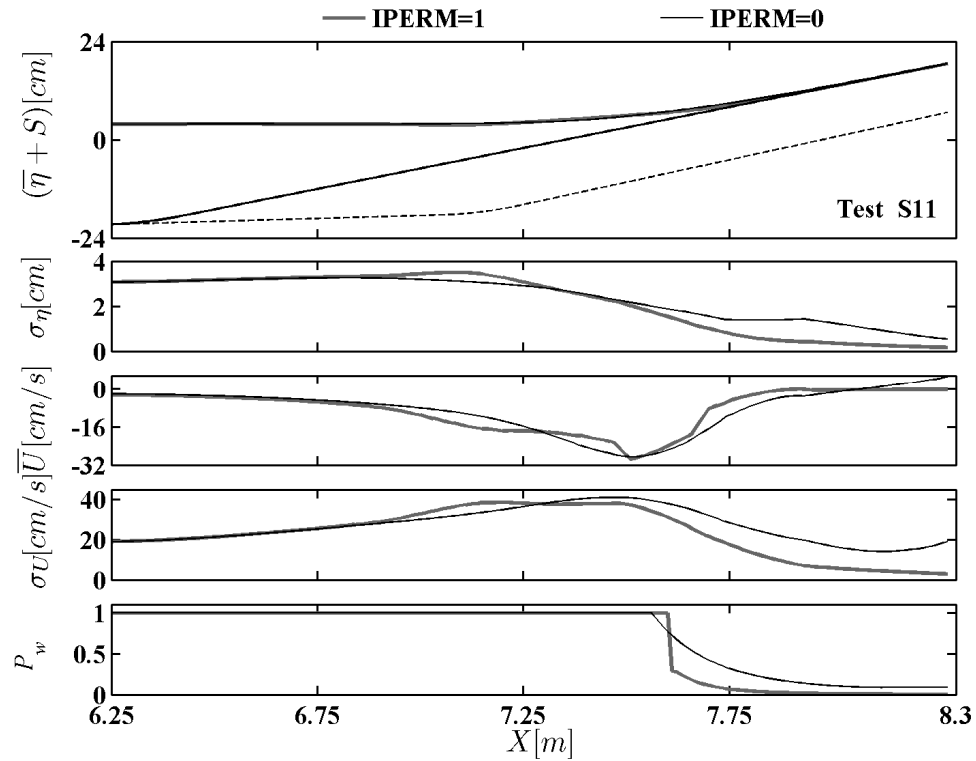


Fig. 3-25. Comparison of mean water level, free surface standard deviation, mean velocity, velocity standard deviation and wet probability for permeable and impermeable bottoms for S11 test

The comparison for OS3 test shown in Fig. 3-26 is similar to that for S11 test because of the thick permeable layer for both test series. In short, the differences between the permeable and impermeable bottoms are apparent above the shoreline of the thick permeable layer.

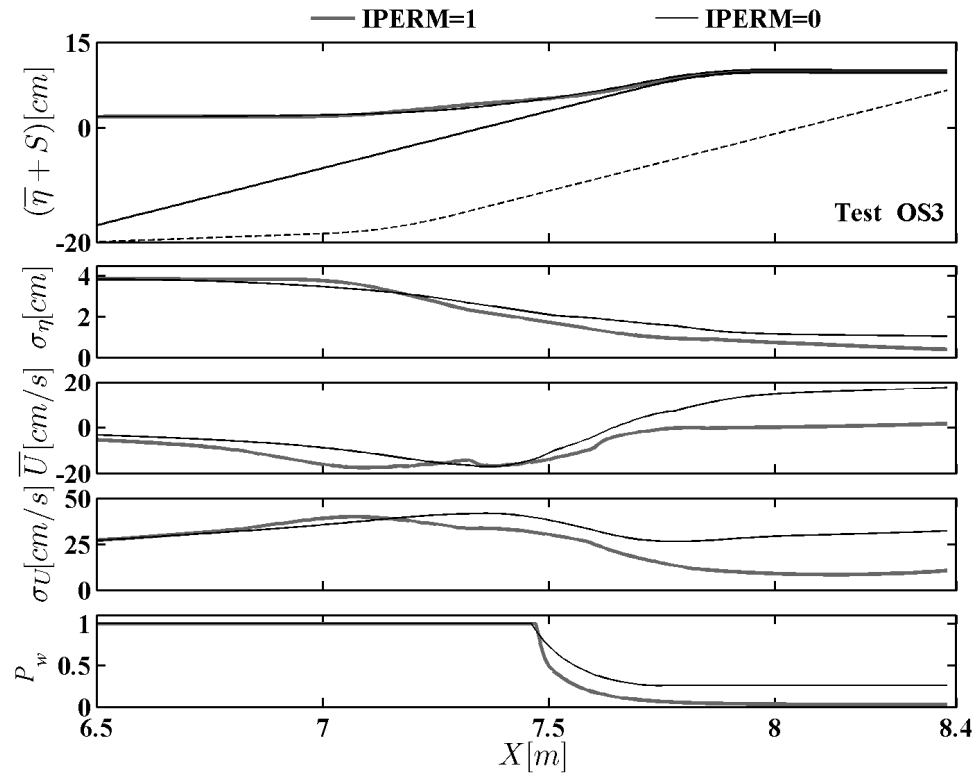


Fig. 3-26. Comparison of mean water level, free surface standard deviation, mean velocity, velocity standard deviation and wet probability for permeable and impermeable bottoms for OS3 test

Fig. 3-27 shows the same comparison for O9 test. The thickness of the permeable layer for O test series is larger than that for D' test series but smaller than those for S and OS test series. Consequently, the permeability effect in Fig. 3-26 is between those for the thin and thick permeable layers as expected physically.

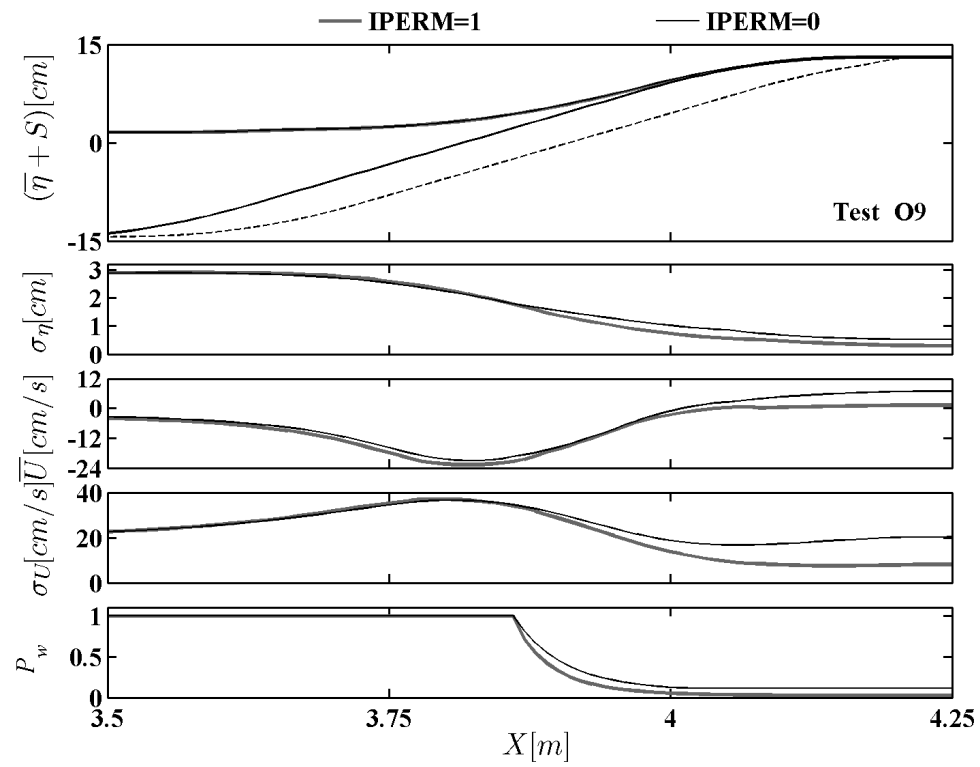


Fig. 3-27. Comparison of mean water level, free surface standard deviation, mean velocity, velocity standard deviation and wet probability for permeable and impermeable bottoms for O9 test

# CHAPTER 4

## DAMAGE PROGRESSION MODEL FOR ARMOR LAYER

The sediment transport model for the wet zone developed by Kobayashi et al. (2009) is modified to predict the movement of stone armor units on a coastal structure. The probability  $P_b$  of stone movement under the Gaussian velocity  $U$  in the wet zone is estimated assuming that the stone movement occurs when the absolute value of the instantaneous velocity  $U$  exceeds the critical velocity  $U_{cb}$  estimated as

$$U_{cb} = [N_c g (s - 1) D_{n50}]^{0.5} \quad (4-1)$$

where  $s$  and  $D_{n50}$  = specific gravity and nominal diameter of the stone; and  $N_c$  = empirical parameter. If the wave height  $H_c$  corresponding to  $U_{bc}$  is given by  $H_c = U_{bc}^2 / g$ , Eq. (4-1) yields

$$N_c = H_c / [(s - 1) D_{n50}] \quad (4-2)$$

where  $N_c$  may be regarded as the critical stability number for the stone which is of the order of unity (Kobayashi et al. 2003). Kobayashi et al. (2009) used the critical Shields parameter  $\Psi_c = 0.05$  for the initiation of sand movement. The two parameters are related by  $N_c = 2\Psi_c / f_b$  and the equation of the probability  $P_b$  given by Kobayashi et al. (2009) is applicable using  $\Psi_c = 0.5 f_b N_c$ . Eq. (4-2) is adopted here and  $N_c$  is calibrated as  $N_c = 0.7$  using the damage progression tests of a stone structure with  $s = 2.66$  and  $D_{n50} = 3.64$  cm conducted by Melby and Kobayashi (1998) which is explained in Chapter 5. The probability of stone suspension is estimated in the same way as in Kobayashi et al. (2009) where the stone fall velocity  $w_f$  is estimated for a sphere (e.g., Jiménez and Madsen 2003) as

$$w_f = 1.8 \left[ g (s - 1) D_{n50} \right]^{0.5} \quad (4-3)$$

For the stone with  $s = 2.66$  and  $D_{n50} = 3.64$  cm,  $w_f = 1.4$  m/s and the computed probability of suspension of this stone is essentially zero. The stone armor units are assumed to move like bed load particles in the following.

The probability  $P_b$  of stone movement in the wet and dry zone is obtained for the probability distribution of  $U$  based on Eqs. (2-15) and (2-18). The probability  $P_b$  of stone movement assumed to be the same as the probability of  $|U| > U_{cb}$  with  $U_{cb}$  given by Eq. (4-1) and is estimated as

$$P_b = P_w \quad \text{for } U_s > U_{cb} \quad (4-4)$$

$$P_b = P_w \exp\left[-\frac{P_w (U_{cb} - U_s)^2}{\alpha^2 g \bar{h}}\right] \quad \text{for } |U_s| \leq U_{cb} \quad (4-5)$$

$$P_b = P_w \left\{ 1 - \exp\left[-\frac{P_w (U_{cb} + U_s)^2}{\alpha^2 g \bar{h}}\right] + \exp\left[-\frac{P_w (U_{cb} - U_s)^2}{\alpha^2 g \bar{h}}\right] \right\} \quad \text{for } -U_s > U_{cb} \quad (4-6)$$

where the upper limit of  $P_b$  is the wet probability  $P_w$  because no stone movement occurs during the dry duration.

The time-averaged volumetric rate  $q_b$  of stone transport is estimated using the formula for bed load in the wet zone proposed by Kobayashi et al. (2009)

$$q_b = b P_b G_s B_r \sigma_U^3 / [g(s-1)] \quad ; \quad B_r = \left( \frac{z_b - z_p}{D_{n50}} \right)^m \leq 1 \quad (4-7)$$

with

$$G_s = \tan \varphi / (\tan \varphi + S_b) \quad \text{for } -\tan \varphi < S_b < 0 \quad (4-8)$$

$$G_s = (\tan \varphi - 2S_b) / (\tan \varphi - S_b) \quad \text{for } 0 < S_b < \tan \varphi \quad (4-9)$$

where  $b$  = bed load parameter;  $G_s$  = function of the bottom slope  $S_b = \partial z_b / \partial x$ , as shown in Fig. 4-1;  $B_r$  = reduction factor due to limited stone availability;  $m$  = empirical parameter;  $\sigma_U$  = velocity standard deviation representing the wave action on the stone; and  $\tan \varphi$  = limiting slope of the stone. The rate  $q_b$  becomes negative (offshore) on the steep slope of

$S_b > (\tan \varphi / 2)$  and  $G_s < 0$ . Use is simply made of  $b = 0.002$  and  $\tan \varphi = 0.63$  adopted by Kobayashi et al. (2009). The reduction factor  $B_r$  is added here to account for the thickness  $(z_b - z_p)$  of the stone layer where  $B_r = 1$  if  $(z_b - z_p) > D_{n50}$  and  $B_r = 0$  in the zone of  $z_b = z_p$  and no stone. The computed profile changes are found to be insensitive to the parameter  $m$  in the range of 0.5 to 2.0 as explained in Chapter 5. The rate  $q_b$  of stone transport in the wet and dry zone is also estimated using Eq. (4-7) where the parameter  $b$  is chosen so that the values of  $q_b$  computed for the two different zones are the same at the still water shoreline located at  $x = x_{\text{SWL}}$ . The computed cross-shore variations of  $q_b$  in the two zones are averaged in the overlapping zone of  $x_{\text{SWL}} \leq x \leq x_r$  for the smooth transition between the two zones.

Finally, the temporal change of the bottom elevation  $z_b$  is computed using the conservation equation of stone volume per unit width

$$(1 - n_p) \frac{\partial z_b}{\partial t} + \frac{\partial q_b}{\partial x} = 0 \quad (4-10)$$

where  $t$  = slow time for the profile change; and  $n_p$  = stone porosity which is assumed to remain constant. Eq. (4-10) is solved numerically to obtain the bottom elevation  $z_b$  at the next time level (Kobayashi et al. 2009). The condition of  $\partial q_b / \partial x = 0$  is imposed at the landward end of the computation domain. This computation procedure is repeated starting from the initial bottom profile until the end of a profile evolution test. The computation time is of the order of  $10^{-3}$  of the test duration.

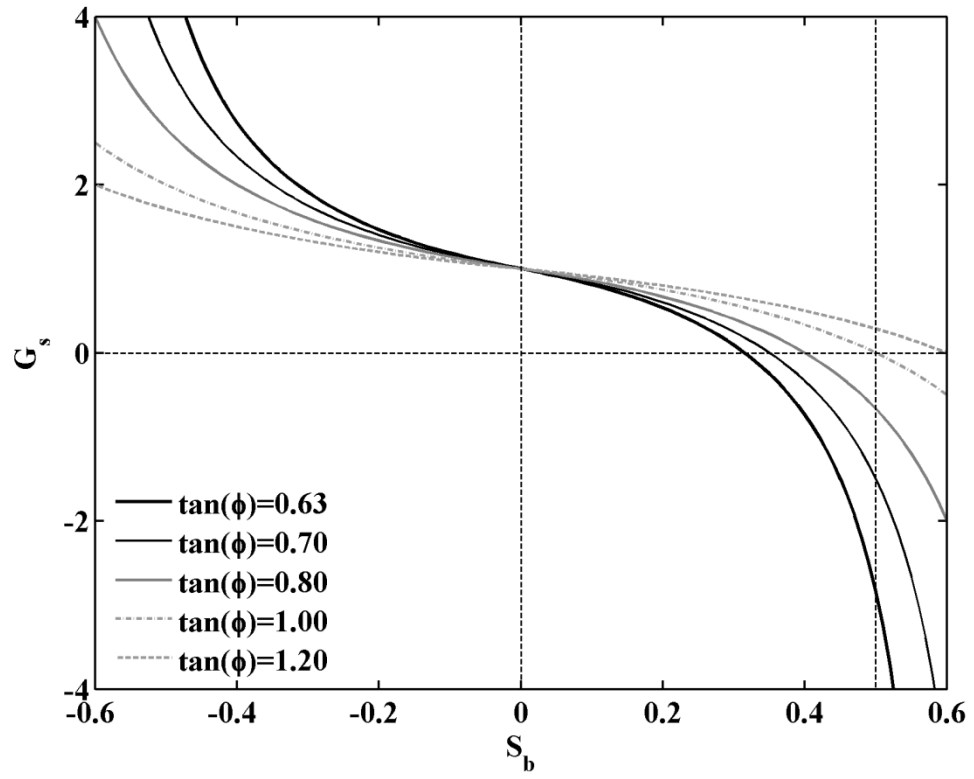


Fig. 4-1. Bottom slope function  $G_s$  versus bottom slope

# **CHAPTER 5**

## **COMPARISON OF DAMAGE PROGRESSION**

### **MODEL WITH DATA**

To evaluate the damage progression model performance, the comparison is made with the damage progression tests for a rubble mound structure by Melby and Kobayashi (1998). The stone structure damage progression tests include three tests A', B' and C' with an identical structure profile and stone but different water levels, wave conditions and durations. The tests were designed to examine the long-term progression of the armor layer damage of a stone structure.

#### **5.1. Experiment by Melby and Kobayashi**

The experiment was conducted in a flume of 61.1 m long, 1.52 m wide, and 2.0 m high. Fig. 5-1 shows the structure cross section. The beach slope was 1/20. The height of the rubble mound structure was 30.5 cm above the toe of the seaward slope of 1/2. The crest width was 11 cm. The armor stone was placed in a traditional two-layer thickness. The armor stone was

characterized by  $D_{n50} = 3.64$  cm,  $s = 2.66$  and  $n_p = 0.4$  where the maximum seepage velocity is  $w_m = 8.7$  cm/s estimated using Eq. (2-14). The thickness of the armor layer was 7.3 cm. The underlayer was 2.9-cm thick and consisted of stone in the size range of 1.27 – 1.59 cm. The size of the core stone ranged from 0.47 to 0.67 cm.

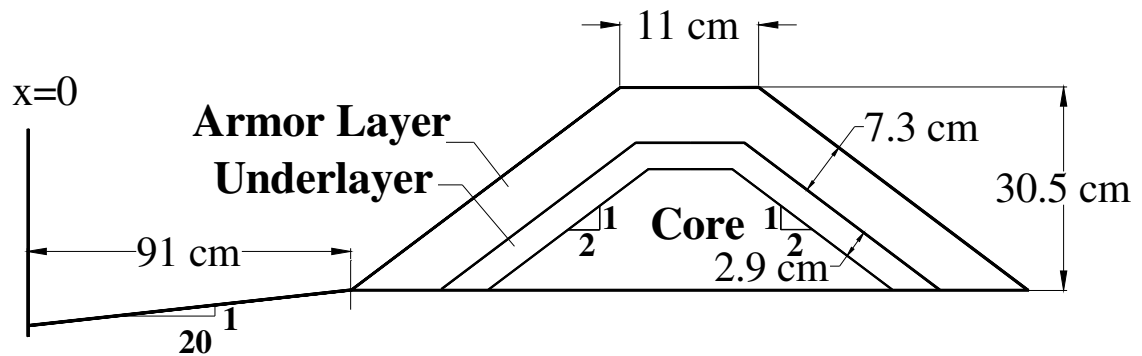


Fig. 5-1. Experimental setup for damage progression tests

The still water depth below  $z=0$  was 11.9 cm at the toe of the slope of 1/2. Table 5-1 summarizes the still water level  $S$  and wave conditions measured at the boundary  $x = 0$  in Fig. 5-1. The time  $t$  is the damage progression time starting from zero damage at  $t = 0$ . The RMS wave height  $H_{rms}$  was increased during constant  $S$ . The profiles were measured along 16 or 32 cross-shore lines every 0.5 h. The average profiles are used here. The tests durations were  $t_e = 28.5, 8.5$  and  $9.0$  h for tests A', B' and C', respectively. The profile was not measured seaward of the toe of the armor layer and on the lower part of the landward slope.

Table 5-1. Still Water Level and Wave Conditions at  $x = 0$  for Three Damage Progression Tests

Test	$t$ (h)	$S$ (cm)	$T_p$ (s)	$H_{rms}$ (cm)
A'	0.0 – 10.5	0.0	2.48	6.9 – 10.0
	10.5 – 28.5	3.9	2.59	7.4 – 11.2
B'	0.0 – 4.5	0.0	2.48	6.9 – 10.0
	4.5 – 8.5	3.9	2.59	9.6 – 11.2
C'	0.0 – 5.0	3.9	2.59	7.4 – 11.2
	5.0 – 9.0	0.0	2.48	8.8 – 10.0

## 5.2. Model Calibration

The damage progression model needs to be calibrated because of the empirical parameters introduced in the model. In Eq. (4-7), the reduction factor  $B_r$  is introduced with the empirical parameter  $m$ . The model is relatively insensitive to the parameter  $m$  in the range of 0.5-2. Figs. 5-2 to 5-4 show the final computed armor profiles for tests A', B' and C' for  $m = 0.5, 1.0$  and  $2.0$  where the calibrated critical stability number  $N_c$  is used. The initial upper and lower boundaries of the armor layer are shown in thin light dash lines. The computed profiles for the different values of  $m$  are very similar. In Fig. 5-5, the temporal variation of the eroded area  $A_e$  is compared using damage  $S_e$  defined as  $S_e = A_e / D_{n50}^2$  for tests A', B' and C' for the different values of  $m$ . The temporal variations of the damage are almost identical for the different  $m$ . Therefore,  $m$  is taken as  $m = 1$  for simplicity.

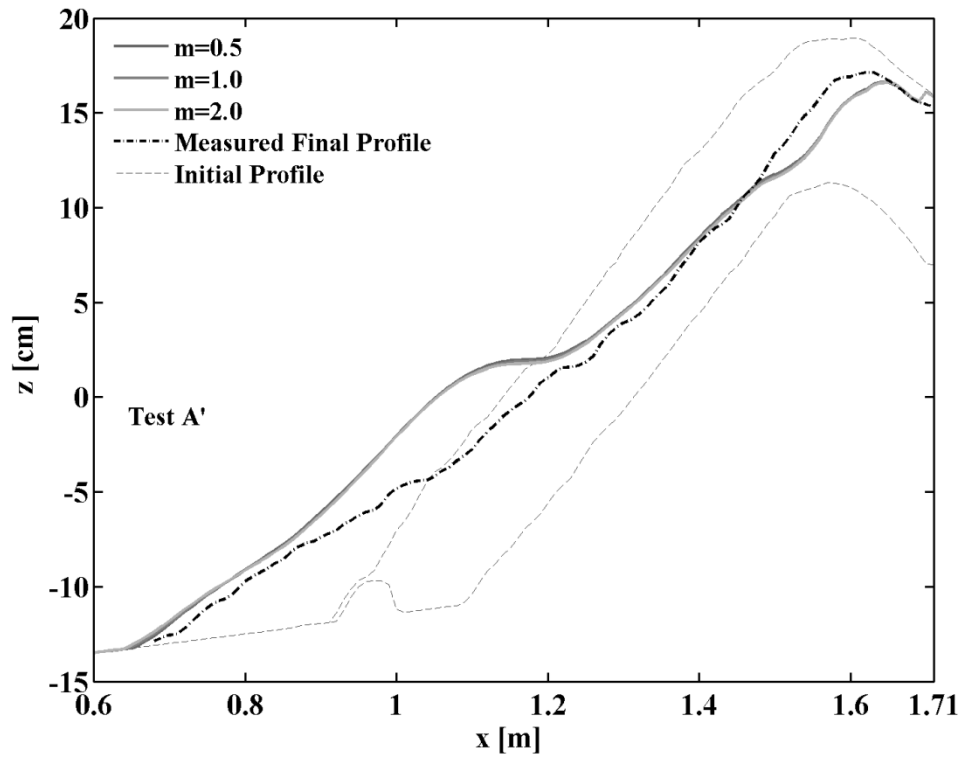


Fig. 5-2. Comparison of final damage profile for test A', for  $m = 0.5, 1$  and  $2$

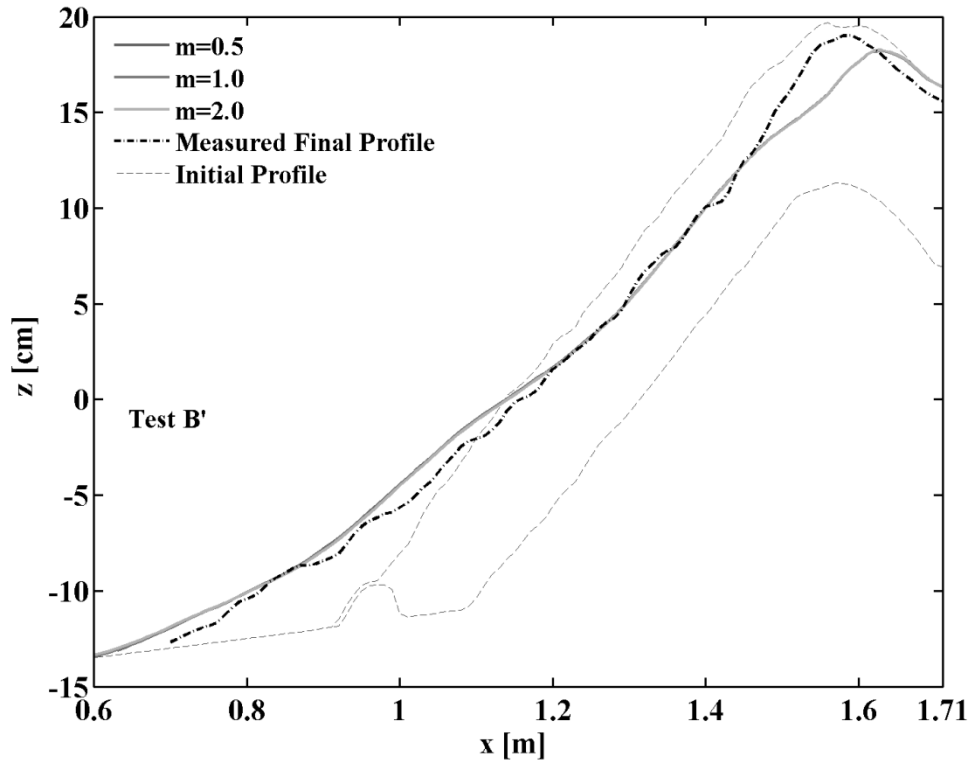


Fig. 5-3. Comparison of final damage profile for test B', for  $m = 0.5, 1$  and  $2$

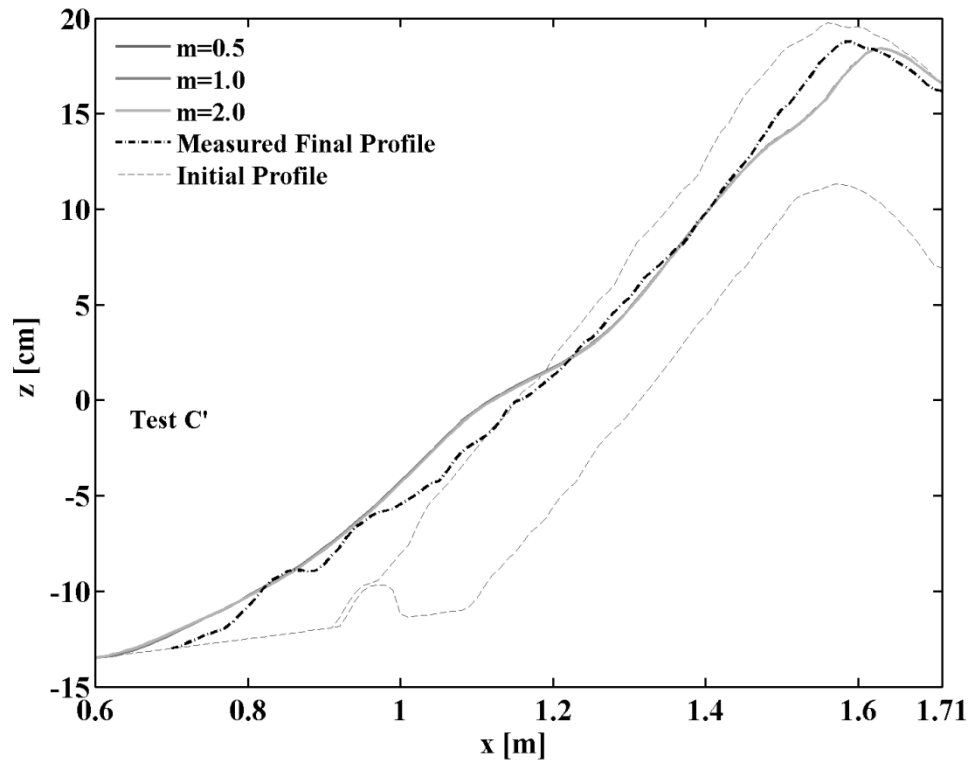


Fig. 5-4. Comparison of final damage profile for test C', for  $m = 0.5, 1$  and  $2$

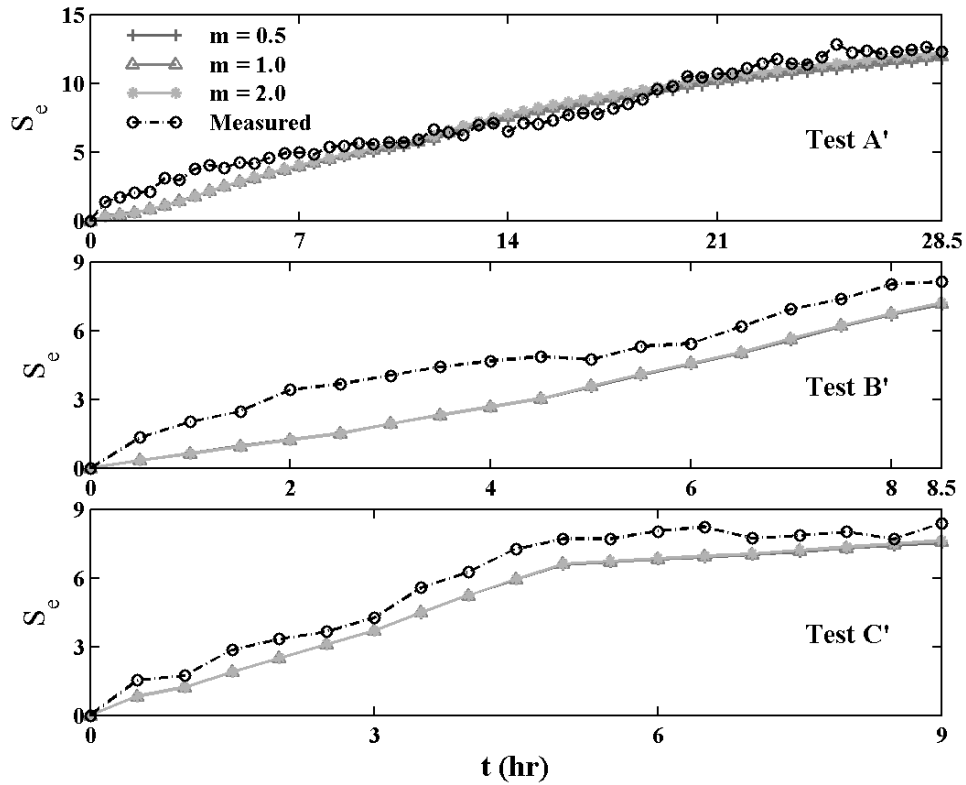


Fig. 5-5. Damage progression for tests A', B' and C' for  $m = 0.5, 1$  and  $2$

As discussed in Chapter 4, the main empirical parameter in the damage progression model is the critical stability number  $N_c$  which needs to be calibrated because the simple criterion of stone movement based on Eq. (4-1) is adopted here to predict the damage progression. To examine the sensitivity of the model to  $N_c$ , computation is made for the three tests using different values of  $N_c$ . Figs. 5-6, 5-7 and 5-8 depict the final computed armor profiles for tests A', B' and C' for  $N_c = 0.6, 0.7$  and  $0.8$ . The critical velocity  $U_{cb}$  for the stone movement increases with the increase of  $N_c$ . Therefore, more damage is predicted with  $N_c = 0.6$  than with  $N_c = 0.8$  in Figs. 5-6 to 5-8. Fig. 5-9 shows the temporal variation

of the damage for tests A', B' and C' for the different values of the critical stability number  $N_c$ . The best agreement with the measured damage progression is achieved for  $N_c = 0.6$ . However, the damage profiles for tests A', B' and C' are predicted better for  $N_c = 0.7$ .  $N_c = 0.7$  is used in the following.

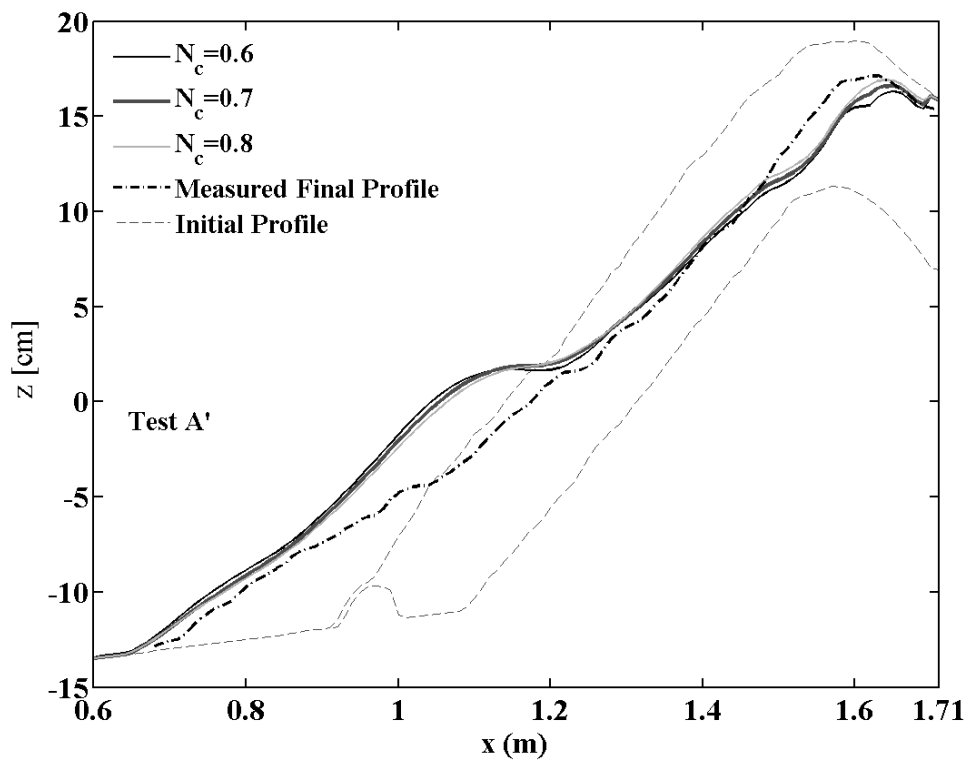


Fig. 5-6. Comparison of final damage profile for test A', for  $N_c = 0.6, 0.7$  and  $0.8$

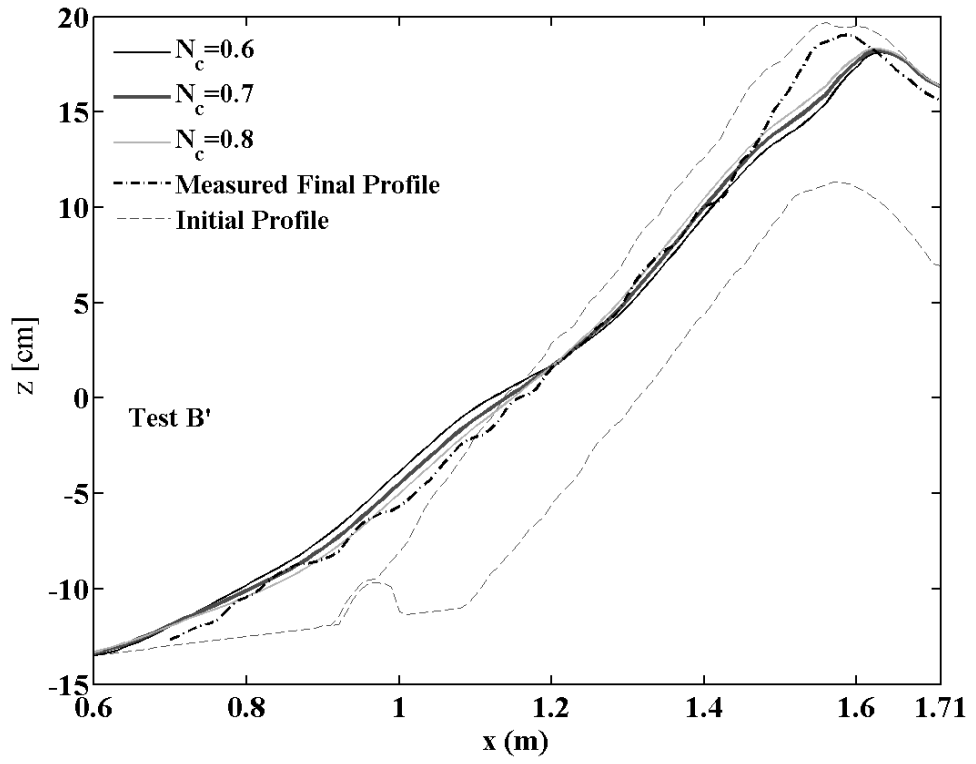


Fig. 5-7. Comparison of final damage profile for test B', for  $N_c = 0.6, 0.7$  and  $0.8$

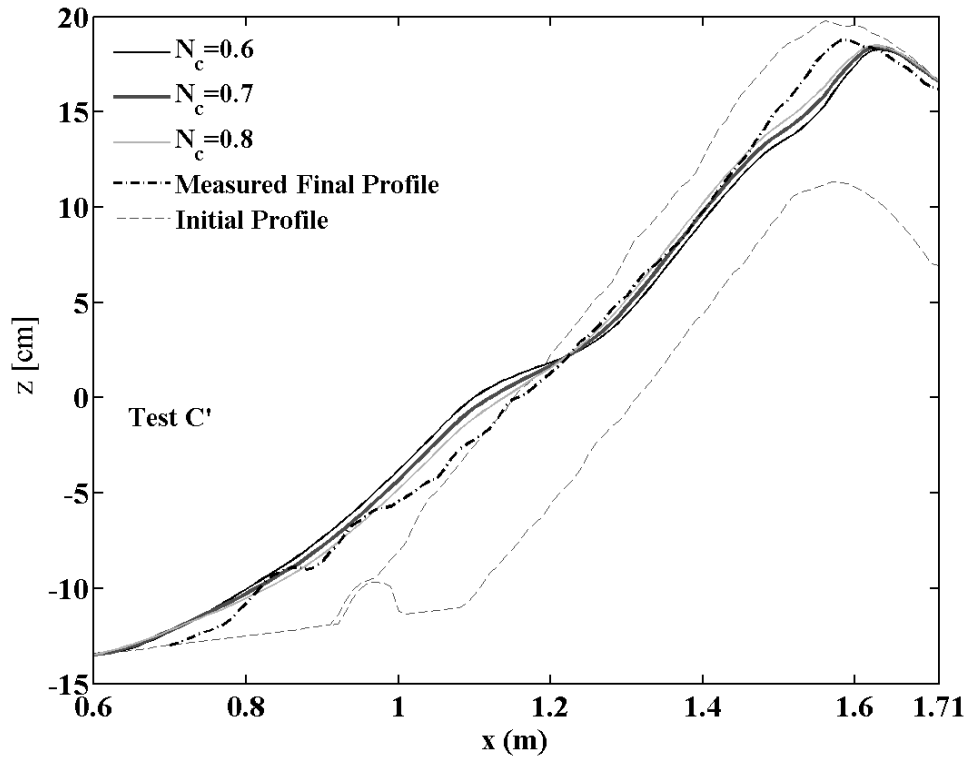


Fig. 5-8. Comparison of final damage profile for test C', for  $N_c = 0.6, 0.7$  and  $0.8$

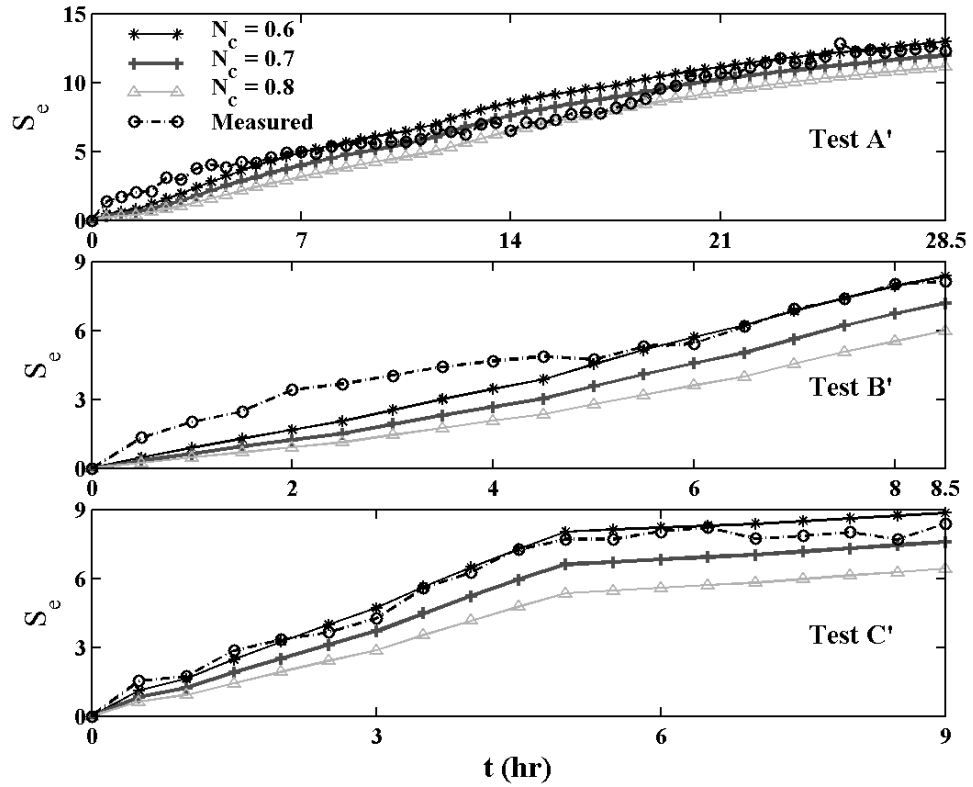


Fig. 5-9. Damage progression for tests A', B' and C' for  $N_c = 0.6, 0.7$  and  $0.8$

#### 5.4. Comparison with Damage Tests

The calibrated damage model is compared with the experiment by Melby and Kobayashi (1998). Computation is made by taking  $z_p$  at the lower boundary of the underlayer as well as the armor layer in Fig. 5-1 to examine the effect of the permeable layer thickness. The difference of the computed results is found to be much smaller than the difference between the measured and computed results presented in this report. Therefore, the assumed impermeable boundary at  $z = z_p$  is taken at the lower boundary of

the armor layer. The measured and computed profiles  $z_b(x)$  at the different time levels (see Table 5-1) are compared in Fig. 5-10 to 5-12 for tests A', B' and C', respectively. As it can be discerned from the figures, the numerical model overpredicts the deposited area below SWL mostly because it does not account for discrete stone units dislodged and deposited at a distance seaward of the toe of the damaged armor layer. The eroded area above SWL is predicted better.

The temporal variations of the damage  $S_e$ , overtopping rate  $q_o$ , root-mean-square wave height  $H_{rms}$  and still water level  $S$ , for test A', B' and C' are plotted in Fig. 5-13 to 5-15. The numerical model predicts the damage progression well partly because the critical stability number  $N_c$  introduced in Eq. (4-1) is calibrated to be  $N_c = 0.7$  for these damage progression tests. The computed wave overtopping rates  $q_o$  suggest that even though the wave overtopping rate is affected by the damage progression, the still water level and wave height at  $x = 0$  are more influential. However, the wave overtopping rate was not measured in this experiment.

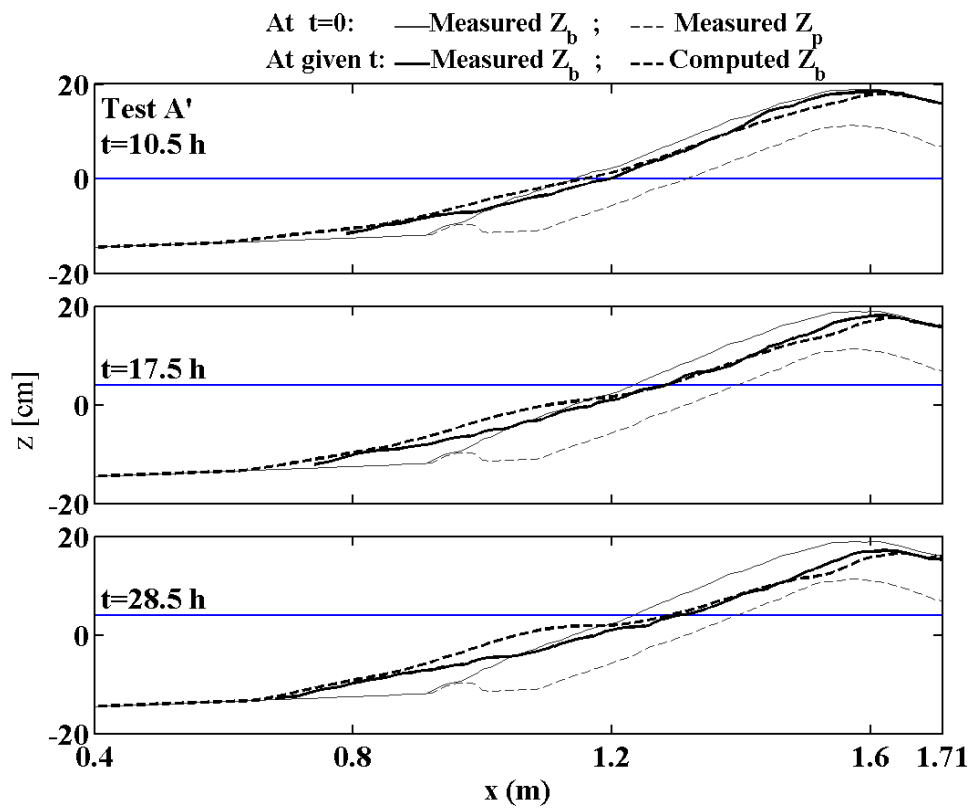


Fig. 5-10. Measured and computed damage profile for test A' at  $t = 10.5$  h,  $17.5$  h and  $28.5$  h

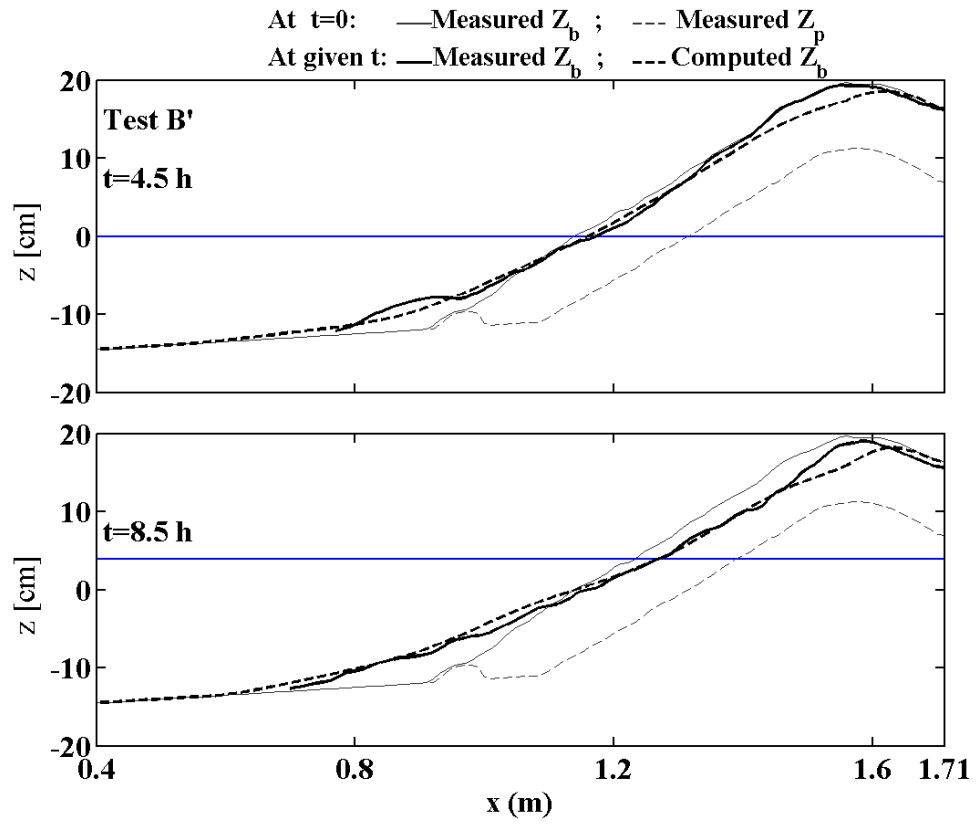


Fig. 5-11. Measured and computed damage profile for test B' at  $t = 4.5$  h and  $8.5$  h

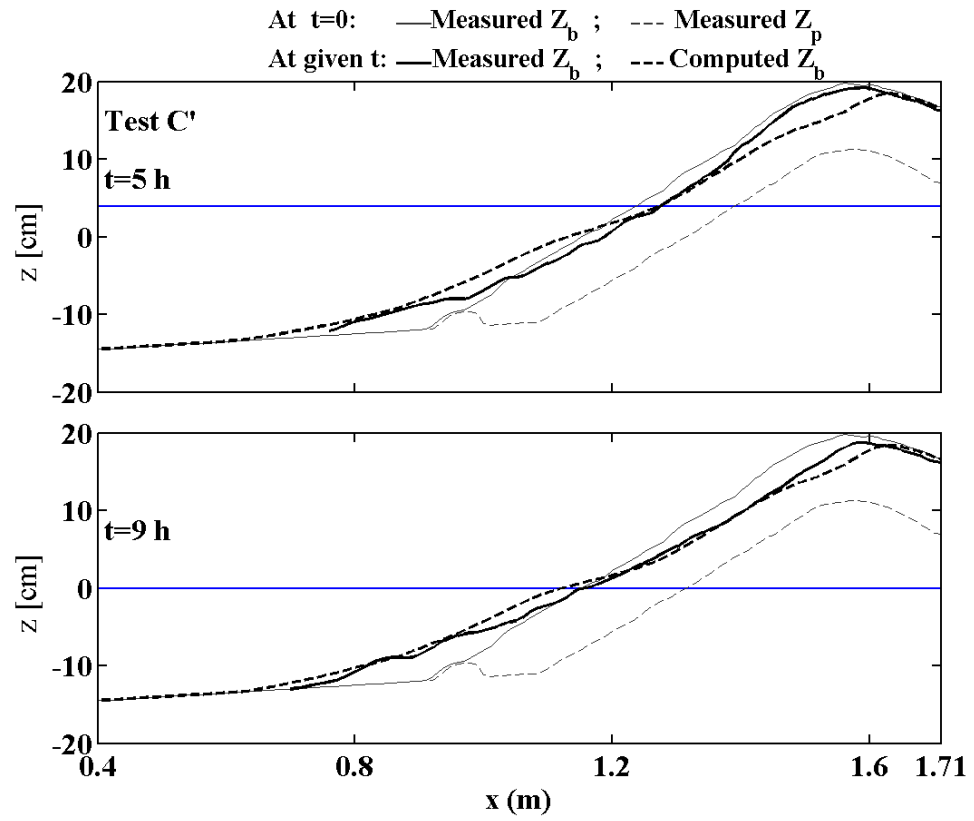


Fig. 5-12. Measured and computed damage profile for test C' at  $t = 5 h$  and  $9 h$

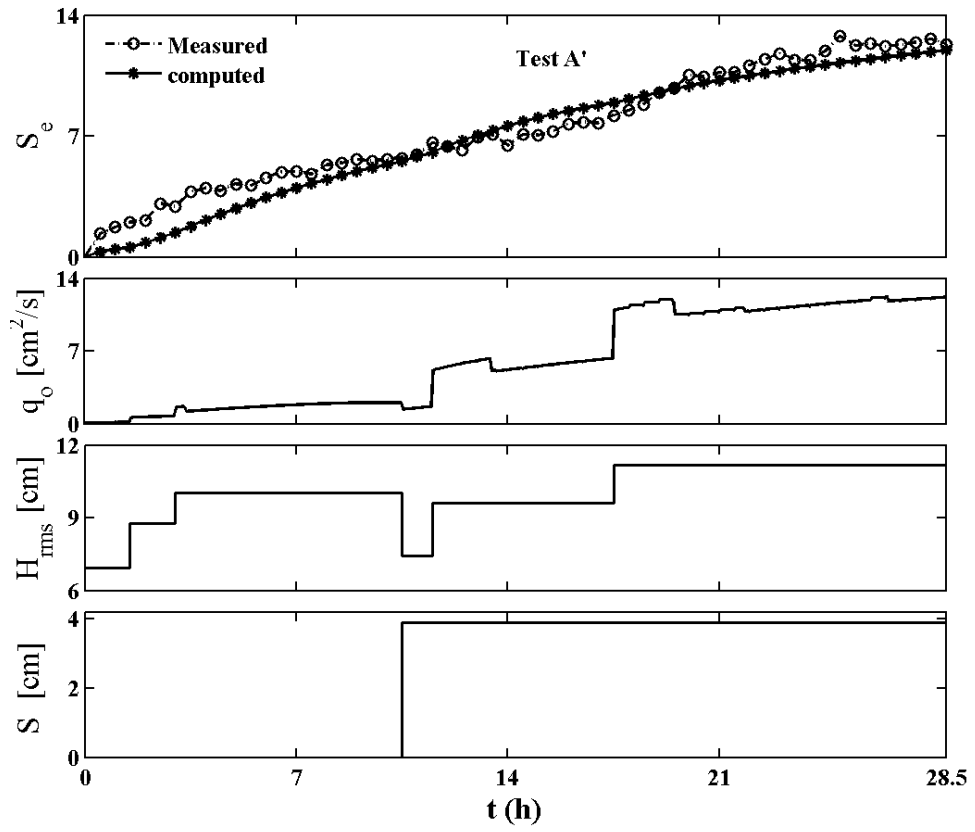


Fig.5-13. Temporal variations of damage, overtopping rate, root-mean-square wave height and still water level for test A'

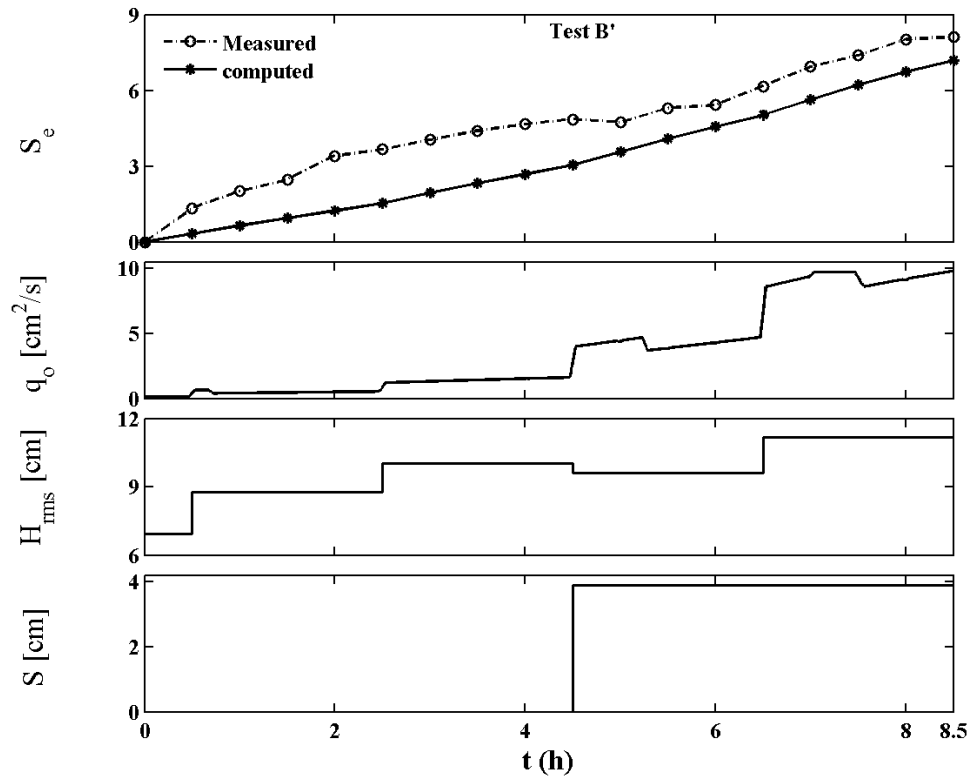


Fig.5-14. Temporal variations of damage, overtopping rate, root-mean-square wave height and still water level for test B'

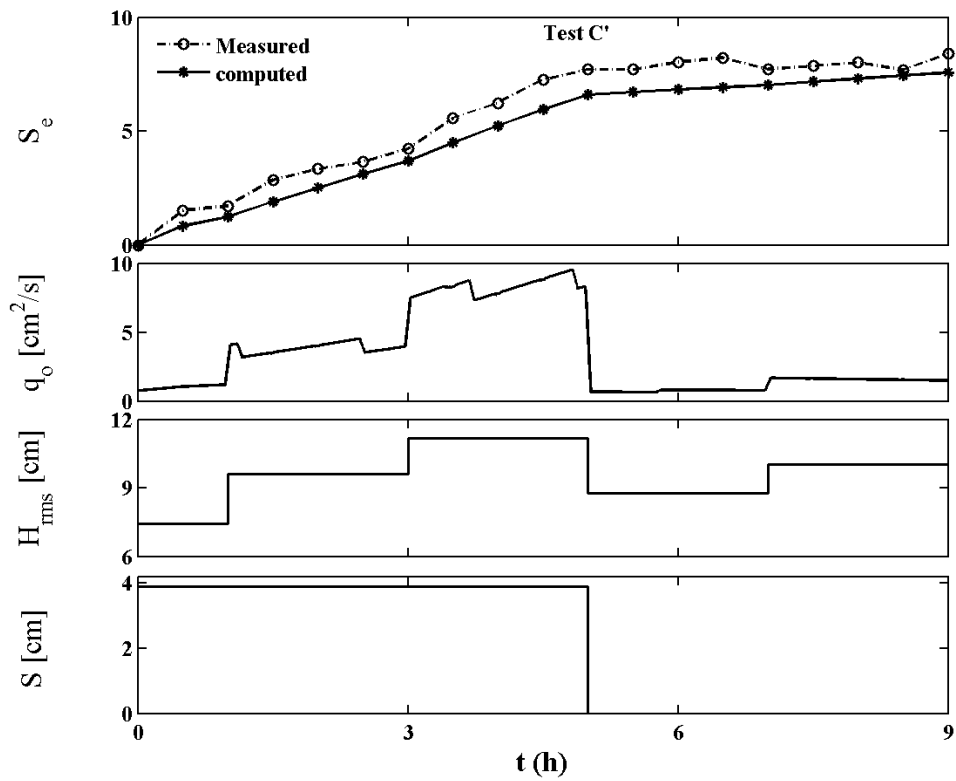


Fig.5-15. Temporal variations of damage, overtopping rate, root-mean-square wave height and still water level for test C'

Figs 5-16 to 5-18 show the computed evolution of the armor layer for the entire duration for tests A', B' and C'. The computational time was of the order of one minute for test A' with the longest duration.

It should be noted that the numerical model needs to be calibrated and verified for the different types of armor units using additional damage tests.

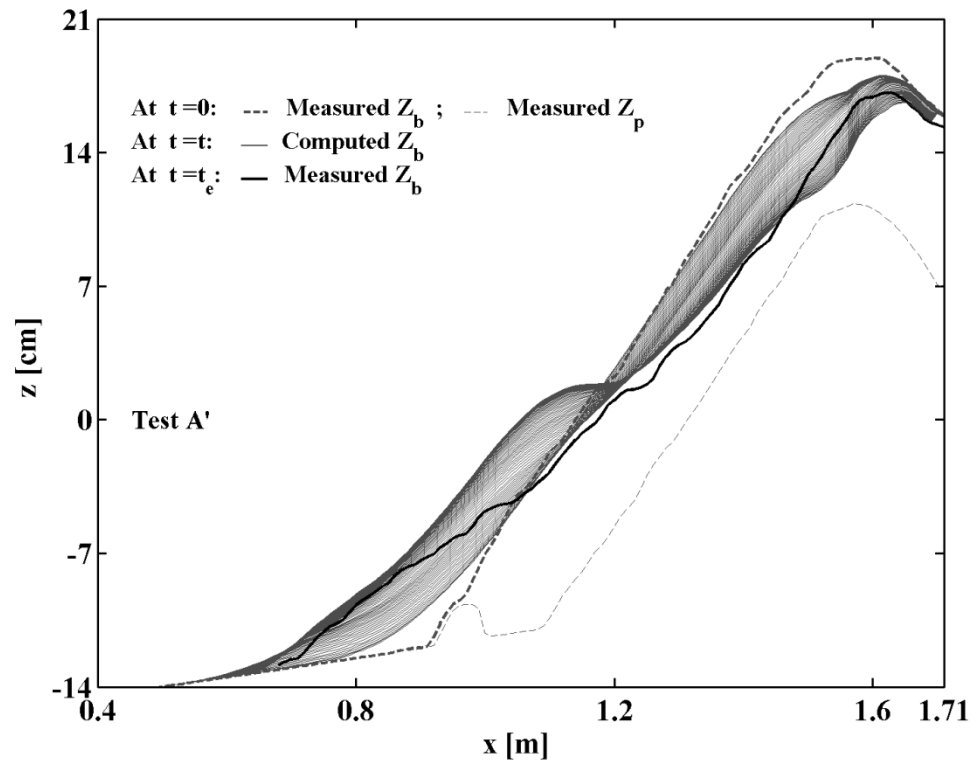


Fig.5-16. Armor profile evolution for test A'

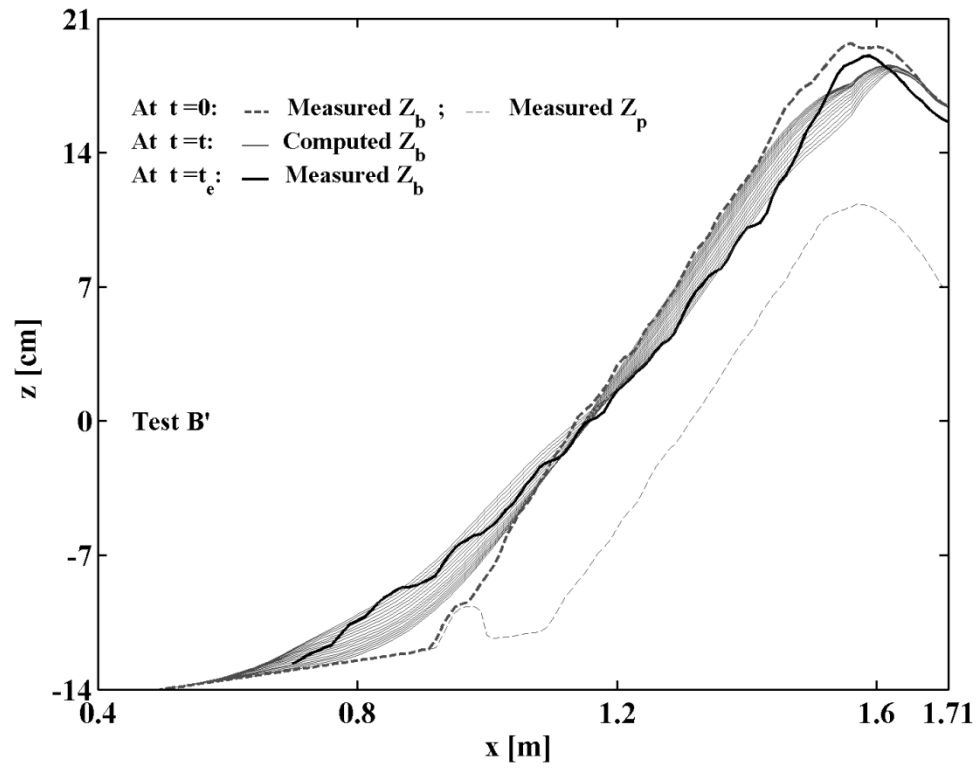


Fig.5-17. Armor profile evolution for test B'

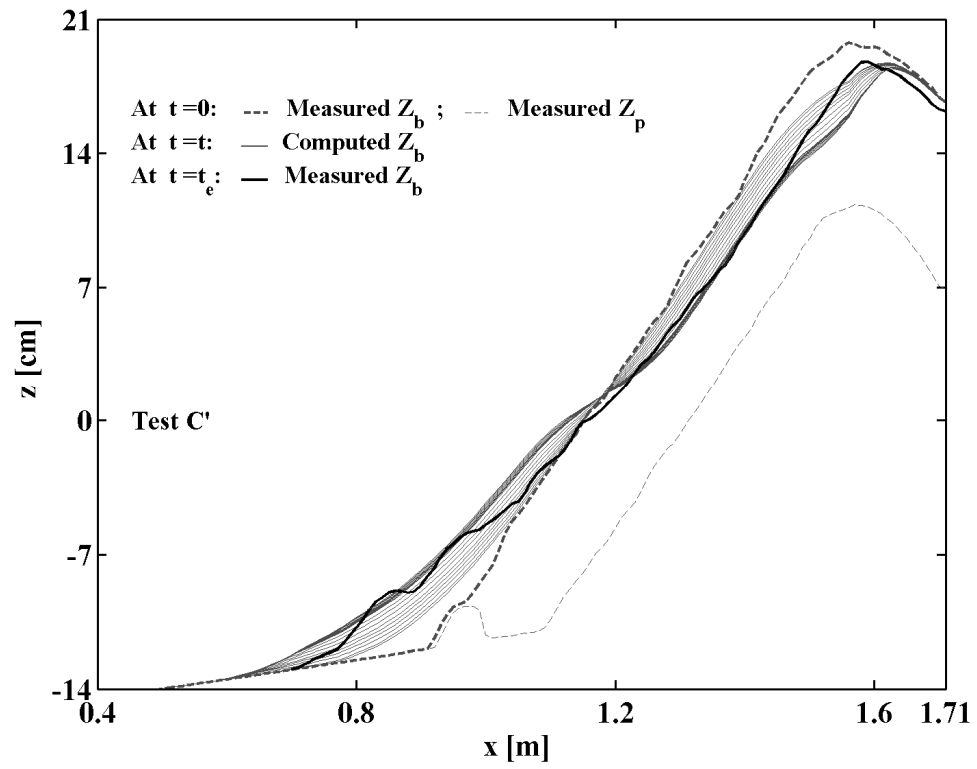


Fig.5-18. Armor layer evolution for test C'

## **CHAPTER 6**

### **CONCLUSIONS**

A probabilistic hydrodynamic model for the wet and dry zone on a permeable structure is developed and connected with the model for the wet zone developed by Kobayashi et al. (2007) which is modified to account for onshore current induced by wave overtopping. The new model for the permeable wet and dry zone is based on the time-averaged continuity and momentum equations for nonlinear shallow-water waves coupled with the assumptions of the exponential probability distribution of the water depth  $h$  given by Eq. (2-15) and the relation given by Eq. (2-18) between the horizontal velocity  $U$  and  $h$ . This model predicts the cross-shore variations of the mean and standard deviation of  $h$  and  $U$  and the wet probability  $P_w$ . The comparison of the developed hydrodynamic model with 52 wave overtopping tests shows that the model predicts the wave overtopping rate and probability and the water depth, velocity and discharge exceeded by 2% of incident 1,000 waves within a factor of about 2. Nevertheless, data will be needed to evaluate the accuracy of Eqs. (2-15) and (2-18) directly.

Damage progression of a rubble mound structure is predicted by modifying the bed load formula proposed by Kobayashi et al. (2009) with input from the hydrodynamic model. The probability  $P_b$  of stone movement is estimated using the critical velocity expressed by Eq. (4-

1) which may be improved with the measurement of the individual stone movement and corresponding fluid velocity. The damage progression model is compared with three tests that lasted up to 28.5 hours. The model predicts the eroded area of the damaged armor layer but underpredicts the deposited area because it does not account for discrete stone armor units dislodged and deposited at a distance seaward of the toe of the damaged armor layer. The temporal variation of the eroded area is predicted well partly because Eq. (4-1) is calibrated for these three tests. The damage progression model will need to be verified using additional damage progression tests for different stone units and other armor units.

## REFERENCES

- Coastal Engineering Manual. (2003). Coastal and Hydraulics Lab., US Army Engineer Research and Development Center, Vicksburg, Miss.
- Farhadzadeh, A., Kobayashi, N. and Melby, J.A. (2010). “Evolution of Damaged Armor Layer Profile”. Coastal Engineering 2010, Proc. 32<sup>nd</sup> Coastal Engineering Conf., World Scientific (will be presented).
- Farhadzadeh, A., Kobayashi, N., Melby, J.A., and Ricottilli, C.(2007). “Experiments and numerical modeling of wave overtopping and overflow on dikes”. Research Report No. CACR-07-02, Center for Applied Coastal Research, Univ. of Delaware.
- Holland, K.T., Holman, R.A., and Sallenger, A.H., Jr. (1991). “Estimation of overwash bore velocities using video techniques.” Proc. Coastal Sediments’91, ASCE, Reston, Va., 489-497.
- Jiménez, J.A., and Madsen, O.S. (2003). “A simple formula to estimate settling velocity of natural sediments.” J. Waterway, Port, Coastal, Ocean Eng., 129(2), 70-78.

- Kobayashi, N., and de los Santos, F.J. (2007). "Irregular wave seepage and overtopping of permeable slopes." *J. Waterway, Port, Coastal, Ocean Eng.*, 133(4), 245-254.
- Kobayashi, N., and Otta, A.K. (1987). "Hydraulic stability analysis of armor units." *J. Waterway, Port, Coastal, Ocean Eng.*, 113(2), 171-186.
- Kobayashi, N., and Farhadzadeh, A. (2008). "Cross-shore numerical model CSHORE for waves, currents, sediment transport and beach profile evolution." Research Rep. No. CACR-08-01, Center for Applied Coastal Research, Univ. of Delaware, Newark, Del.
- Kobayashi, N., Pozueta, B., and Melby, J.A. (2003). "Performance of coastal structures against sequences of hurricanes." *J. Waterway, Port, Coastal, Ocean Eng.*, 129(5), 219-228.
- Kobayashi, N., Buck, M., Payo, A., and Johnson, B.D. (2009). "Berm and dune erosion during a storm." *J. Waterway, Port, Coastal, Ocean Eng.*, 135(1), 1-10.
- Kobayashi, N., Herrman, M.N., Johnson, B.D., and Orzech, M.D. (1998). "Probability distribution of surface elevation in surf and swash zones." *J. Waterway, Port, Coastal, Ocean Eng.*, 124(3), 99-107.
- Kobayashi, N., Meigs, L.E., Ota, T., and Melby, J.A. (2007). "Irregular breaking wave transmission over submerged porous breakwaters." *J. Waterway, Port, Coastal, Ocean Eng.*, 133(2), 104-116.
- Kobayashi, N., Farhadzadeh, A., Melby, J.A., Johnson, B., and Gravens, M. (2010). "Wave overtopping of levees and overwash of dunes." *J. Coastal Research* (in press).

- Kobayashi, N., Farhadzadeh, A., and Melby, J.A. (2010). "Wave Overtopping and Damage Progression of Stone Armor Layer". *J. Waterway, Port, Coastal, Ocean Eng.* (submitted)
- Losada, I.J., Lara, J.L., Guanche, R., and Gonzalez-Ondina, J.M. (2008). "Numerical analysis of wave overtopping of rubble mound breakwaters." *Coastal Eng.*, 55, 47-62.
- Mei, C.C. (1989). *The Applied Dynamics of Ocean Surface Waves*. World Scientific, Singapore.
- Melby, J.A., and Kobayashi, N. (1998). "Progression and variability of damage on rubble mound breakwaters." *J. Waterway, Port, Coastal, Ocean Eng.*, 124(6), 286-294.
- Norton, P.A., and Holmes, P. (1992). "Armor displacements on reshaping breakwaters." *Coastal Engineering 1992, Proc. 23rd Coastal Engineering Conf., ASCE, Reston, Va.*, 1448-1460.
- van Gent, M.R.A. (1995). "Porous flow through rubble-mound material." *J. Waterway, Port, Coastal, Ocean Eng.*, 121(3), 176-181.
- van Gent, M.R.A. (2002). "Low-exceedance wave overtopping events: Measurements of velocities and the thickness of water-layers on the crest and inner slope of dikes." *Delft Cluster Report DC 030202/H3802, Delft Hydraulics, Delft, The Netherlands*.
- Wurjanto, A., and Kobayashi, N. (1993). "Irregular wave reflection and runup on permeable slopes." *J. Waterway, Port, Coastal, Ocean Eng.*, 119(5), 537-557.